ORNL/TM-10585

ornl

OAK RIDGE
NATIONAL
LABORATORY

MARTIN MARIETTA

# Nonlinear Evolution of the Internal Kink Mode in Toroidal Geometry for Shaped Tokamak Plasmas

J. A. Holmes
B. A. Carreras
L. A. Charlton
V. E. Lynch
R. J. Hastie
T. C. Hender



OPERATED BY
MARTIN MARIETTA ENERGY SYSTEMS, INC.
FOR THE UNITED STATES
DEPARTMENT OF ENERGY

Printed in the United States of America. Available from
National Technical Information Service
U.S. Department of Commerce
5285 Port Royal Road, Springfield, Virginia 22161
NTIS price codes—Printed Copy: A04; Microfiche A01

ORNL/TM-10585
Dist. Category UC-20 g

Fusion Energy Division

# NONLINEAR EVOLUTION OF THE INTERNAL KINK MODE IN TOROIDAL GEOMETRY FOR SHAPED TOKAMAK PLASMAS

J. A. Holmes
B. A. Carreras
L. A. Charlton
V. E. Lynch
R. J. Hastie*
T. C. Hender*

*Culham Laboratory, Abingdon, Oxon OX14 3DB, England

Date Published — September 1987

Prepared by the
OAK RIDGE NATIONAL LABORATORY
Oak Ridge, Tennessee 37831
operated by
Martin Marietta Energy Systems, Inc.
for the
U.S. DEPARTMENT OF ENERGY
under contract DE-AC05-84OR21400

# CONTENTS

## ABSTRACT

The nonlinear evolution of the internal kink mode is studied in toroidal geometry for noncircular cross section tokamak plasmas. The study is focused on very low shear and hollow $q$ profiles with $q(\rho) \geq 1$ for which the internal kink is unstable, in the latter case even at $\beta = 0$. The nonlinear evolution is dominated by ideal magnetohydrodynamics (MHD), and the instability saturates, giving a quasi-helical shift to the magnetic axis. The nonlinear saturation is caused by increased field line bending. Time scales of $10^3 \tau_{Hp}$ and axis shifts of 20% are reached when changes in $q$ on the order of $3 \times 10^{-3}$ from the marginal profile are produced.


## 1. INTRODUCTION

Understanding the sawtooth oscillation in tokamaks is extremely important because this instability limits confinement at the plasma core. This instability is generally associated with the $m = 1$ mode and the presence of the $q = 1$ surface in the plasma. Despite much experimental, theoretical, and computational effort, the general behavior of the $m = 1$ instability resists complete understanding. Theoretically, this is largely because of its complicated nature in toroidal geometry. Depending on the type of $q$ profile, the Lundquist number $S$, the value of plasma $\beta$, and the aspect ratio, the $m = 1$ instability changes character,[1] taking the form of resistive kink, tearing mode, or ideal kink. Each form corresponds to different linear properties and to a variety of nonlinear behavior, and each leads therefore to different predictions for experimental observations.

Experimentally, a wide variety of phenomena is associated with this instability. In large tokamaks that have low resistivity, the sawtooth crash occurs on a rapid time scale, suggesting an ideal MHD mechanism. For example, the observed sawtooth crash time for JET is about 100 $\mu s$,[2] which is almost two orders of magnitude less than the prediction of Kadomtsev's resistive reconnection model.[3,4] Analysis of a JET fast sawtooth collapse

reveals a rapidly growing $m = 1$ component in the soft X-ray emission and electron temperature profiles.[2]

To explain this rapid sawtooth collapse, Wesson proposed a model in which the ideal $m = 1$ instability is responsible for the crash.[4] According to the model, to generate the sudden, precursorless disruption, such a mode must undergo a sharp transition from ideal stability to vigorous growth, so that slight diffusive changes in profiles can trigger a hard instability. The structure of this instability must also be global enough to induce the observed transition from peaked to hollow emissivity profiles, and it must occur at low plasma $\beta$ consistent with experiment. Because of the rapidity of the crash and the high conductivity of large tokamaks, the collapse is postulated to involve no reconnection. Instead, the hot central plasma is shifted convectively as cooler plasma flows into the center, and together these form a configuration of 1/1 helicity. Reconnection then occurs on a longer resistive time scale after the collapse.

Two types of safety factor profile for which the internal kink is unstable at very low $\beta$ and which lead to sharp linear stability boundaries are hollow (non-monotonic) profiles having an off axis $q_{\min} \approx 1$ and very low shear (flat) profiles with central $q_0 \approx 1$. Slightly hollow profiles have been obtained in transport simulations of sawtooth discharges,[5,6] and very low shear profiles have been measured on ASDEX.[7] By generalizing the linearized analysis of Bussac et al.,[8] it has been shown[1] that both types of profile lead to an ideal instability having sharp stability boundaries at low $\beta$ and eigenfunctions of dominant size in the plasma core.

Analytic calculations demonstrate that the ideal stability properties are strongly dependent on toroidal curvature, even to the extent that at low $\beta$ opposite signs are obtained for $\delta W$ in toroidal and cylindrical geometry. Even so, the nonlinear behavior of the $m = 1$ mode has been examined in cylindrical geometry for very low shear profiles[9,10] and for hollow profiles,[11] with the plasma $\beta$ chosen to provide growth rates commensurate with experimental values. Recently a nonlinear calculation in toroidal geometry has

been published[12] which shows many features in common with the rapid sawtooth. Clearly, systematic nonlinear calculations in toroidal geometry are necessary to gain a detailed understanding of the behavior of the $m = 1$ mode in tokamaks.

This paper first recounts the linear stability properties for hollow and low-shear $q$ profiles with $q(\rho) \geq 1$. The internal kink stability boundary for these profiles is determined by the stabilization caused by field line bending, not by a change in the sign of $\delta W_T$. The effect of plasma cross section shaping is investigated, and the dominant shaping effects on stability come from modification of the field line bending, which changes the stability boundaries.

The main purpose of the paper is to study the nonlinear effects by calculating the time evolution of the instability. This evolution is dominated by ideal MHD dynamics, and the evolution time scale is close to $\gamma^{-1}$, where $\gamma$ is the linear growth rate. The instability nonlinearly saturates at a finite size, causing a helical shift of the magnetic axis and a crescent-shaped distortion of the magnetic surfaces. The increased field line bending caused by this distortion is the cause of the saturation of the instability.

This paper is organized as follows: Sect. 2 discusses the features of the equations and equilibrium of particular interest here; linear stability is the subject of Sect. 3; in Sect. 4 the nonlinear stability results are presented; a discussion of the numerics is given in Sect. 5; and Sect. 6 contains a discussion of the physics results. Finally, conclusions concerning the likelihood that the studies presented here pertain to the rapid sawtooth crash are given in Sect. 7.

## 2. EQUILIBRIUM AND EQUATIONS

This paper examines the nonlinear behavior of the $m = 1$ internal kink instability for circular and noncircular plasmas in toroidal geometry, for both hollow and low-shear profiles in the framework of incompressible MHD. The instability studied in this work is more correctly identified as an $n = 1$ ($n$ is the toroidal mode number) mode because of the

toroidal coupling of the poloidal components $m$. However, for the profiles studied here, the $m = 1$ poloidal component is dominant and the term $m = 1$ instability is generally used. The numerical calculations were done with an incompressible version of the initial value, ideal or resistive fixed boundary, MHD computer code, FAR.[13] The numerical methods used in FAR are discussed in detail in Ref. 13, and solution of the incompressible equations is discussed in Ref. 14. Only a brief discussion of the model will be included here.

The FAR code solves the MHD equations in three spatial dimensions and in time starting from an initial equilibrium solution plus a small perturbation. The spatial part of the problem is represented in a straight-field-line magnetic flux coordinate system of the equilibrium. The coordinates are $(\rho, \theta, \zeta)$, where $0 \leq \rho \leq 1$ is a generalized minor radius flux surface label, $0 \leq \theta \leq 2\pi$ is a generalized poloidal angle, and $0 \leq \zeta \leq 2\pi$ is the toroidal angle. This coordinate system is used to define an average plasma minor radius $a$, which includes the effects of shaping

$$a^2 = \frac{R_0}{2\pi^2} \int R^{-2} d\tau \ , \tag{1}$$

where $R_0$ is the plasma major radius, $R$ is the major radius coordinate, and the volume integral is taken over the entire plasma. Also defined is a shape-dependent inverse aspect ratio $\epsilon = a/R_0$. This inverse aspect ratio is, for shaped plasmas, distinct from the usual tokamak inverse aspect ratio $\epsilon_H = a_H/R_0$, where $a_H$ is the horizontal minor radius. In this paper, we use this notation to distinguish the shape-dependent and usual aspect ratios. Three advantages associated with the use of flux coordinates are the ability to resolve radially localized singular layers, the ability to accurately represent the operator $\vec{B} \cdot \vec{\nabla}$, and the ability to treat shaped plasmas without reformulating the method of solution. The final advantage permits the study of shaping effects simply by varying the shape of the equilibrium cross section.

The equilibrium solution is calculated using the code RSTEQ,[15] which solves the two-dimensional, axisymmetric Grad-Shafranov equation and maps the solution into the desired

flux coordinates. The equilibria used in this paper are determined for a safety factor profile $q(\rho)$ and a pressure profile $p(\psi_{eq})$, where $\psi_{eq}$ is the equilibrium poloidal magnetic flux function. Throughout this work the pressure profile is chosen to be

$$p(\psi_{eq}) = p_0\{[\psi_{eq} - \psi_{eq}(a)]/[\psi_{eq}(0) - \psi_{eq}(a)]\}^2, \tag{2}$$

where $p_0$ is the pressure at the magnetic axis, $\psi_{eq}(0)$ is the value of $\psi_{eq}$ at the magnetic axis, and $\psi_{eq}(a)$ is the value at the plasma edge.

The usual forms of the parameterizations for the equilibrium safety factor profiles used here are:

$$q(\rho) = q_{\min} + \Delta q\left[1 - (\rho/\rho_{\min})^2\right]^2 \tag{3}$$

and

$$q(\rho) = q_0[1 + (\rho/\rho_0)^{2\lambda}]^{1/\lambda} - \Delta q_\ell e^{-\left(\frac{\rho^2-\rho^2_{\min}}{2\rho_{\min}\Delta\rho}\right)^2}. \tag{4}$$

Equation (3) defines a hollow profile of depth $\Delta q$ as measured from the magnetic axis to the minimum $q_{\min}$ at $\rho = \rho_{\min}$. Certain generalizations of this profile will be defined later as they are needed. Equation (4) defines a locally hollow profile with a minimum of depth $\Delta q_\ell$ at $\rho_{\min}$. Near $\rho_{\min}$ this hollow contribution is approximately Gaussian with a width of $\Delta\rho$. In most calculations presented here using Eq. (4), $\Delta q_l$ is chosen to be zero. Then, for appropriate choices of $\rho_0$ and $\lambda$, a low-shear profile results. In this paper the usual parameter choices are $\Delta q = 0.1$, $\rho_{\min} = 0.5$, and $q_{\min} \approx 1.0$ in Eq. (3), and $\Delta q_\ell = 0$, $\lambda = 6$, $\rho_0 = 0.75$, and $q_0 \approx 1.0$ in Eq. (4). Exceptions to these choices will be discussed as they occur. Examples of the hollow and low-shear profiles with the parameter choices defined above are plotted in Fig. 1 together with an example of the locally hollow profile with $\Delta q_\ell = 0.1$, $\lambda = 6$, $\rho_0 = 0.75$, $q_0 = 1.1$, $\rho_{\min} = 0.5$, and $\Delta\rho = 0.1$.

The plasma geometry is given by specifying the major radius $R_0$, the horizontal minor radius $a_H$, which is the distance from $R_0$ to the plasma boundaries on midplane, and a functional form for the plasma boundary. RSTEQ is a fixed boundary equilibrium code that maintains the specified boundary as the outside flux surface, so that $p = 0$ and $\psi_{\rm eq} = \psi_{\rm eq}(a)$ on the boundary. In this paper, we study the effects of plasma elongation and triangularity (D-shaping) on the $m = 1$ internal kink mode by using the following parameterization of the boundary:

$$R = R_0 + a_H \cos(\theta + \delta \sin\theta) \tag{5a}$$

and

$$z = \kappa a_H \sin\theta \ . \tag{5b}$$

In Eq. (5), $z$ is the vertical coordinate, so that $\kappa$ is the plasma elongation and $\delta$ is the triangularity. The maximum height of the boundary is $z_{\rm max} = \kappa a_H$, which occurs at $R = R_0 - a_H \sin\delta$, so that $\sin\delta$ gives the inward shift of the maximum height (relative to $a_H$) caused by $D$ shaping. Choosing $\delta = 0$ results in an elliptical plasma boundary, while $\kappa = 1.0$ and $\delta = 0$ give a circular plasma of radius $a_H$ centered at $R_0$.

The dynamical equations used here are those of MHD with an incompressibility assumption for the velocity

$$\vec{\nabla} \cdot \vec{v} = 0. \tag{6}$$

The magnetic field is represented in terms of the vector potential

$$\vec{B} = \vec{\nabla} \times \vec{A}, \tag{7}$$

which guarantees that $\vec{B}$ is divergence-free. Similarly, the incompressibility assumption is enforced by using a vector stream function

$$\vec{v} = \vec{\nabla} \times \vec{\Phi} \tag{8}$$

to represent the velocity. The magnetic field is evolved by combining Faraday's and Ohm's laws to obtain an equation for the vector potential

$$\frac{\partial \vec{A}}{\partial t} = -\vec{\nabla}\alpha + \vec{v} \times \vec{B} - \frac{\eta}{S}\vec{j} \, , \tag{9}$$

where $\alpha$ is the electrostatic potential, $\vec{j} = \vec{\nabla} \times \vec{B}$ is the current, $\eta$ is the resistivity, and $S = \tau_R/\tau_{\rm Hp}$ is the Lundquist number. Both $\tau_R$, the resistive skin time, and $\tau_{\rm Hp}$, the poloidal Alfvén time, are defined later in the discussion of the system of units for these equations. The velocity is evolved by taking the curl of the momentum equation, which eliminates the $\vec{\nabla}p$ pressure term and decouples the dynamics of the pressure from the momentum and magnetic field evolutions. Then, an evolution equation is obtained for the vector stream function

$$\frac{\partial}{\partial t}(\vec{\nabla} \times \vec{\nabla} \times \vec{\Phi}) = -\vec{\nabla} \times (\vec{v} \cdot \vec{\nabla}\vec{v}) + \vec{\nabla} \times (\vec{j} \times \vec{B}). \tag{10}$$

In obtaining Eq. (10), the mass density $\rho_m = \rho_{m0}$ is assumed to be constant in space and time. This assumption, together with Eq. (6), leads to satisfaction of the continuity equation

$$\frac{\partial \rho_m}{\partial t} + \vec{\nabla} \cdot (\rho_m \vec{v}) = 0 \, . \tag{11}$$

In writing Eqs. (6)–(11), a system of units is used in which lengths are normalized to the generalized minor radius $a$, magnetic fields to the toroidal vacuum field $B_0$ at $R_0$, mass density to the constant value $\rho_{m0}$, and resistivity to the value at the magnetic axis $\eta_0$. In terms of these units, time is expressed in poloidal Alfvén times, $\tau_{Hp} = R_0/v_A$, where $v_A$ is the Alfvén velocity, $v_A = B_0/\sqrt{\mu_0 \rho_{m0}}$, and $\mu_0$ is the vacuum magnetic permeability. The resistive time, which then defines $S$, is given by $\tau_R = \mu_0 a^2/\eta_0$.

By eliminating the equation of continuity, only the two vector equations, Eqs. (9) and (10), must be evolved in time. Although it appears that this requires the solution of six dynamical equations, this number is reduced to five by an appropriate choice of gauge for the potentials $\vec{A}$ and $\vec{\Phi}$. In terms of the flux coordinate representation, a gauge was chosen that had $A_\rho = 0$ and $\Phi_\rho = 0$, where $A_\rho$ and $\Phi_\rho$ were the covariant $\rho$ components of $\vec{A}$ and $\vec{\Phi}$, respectively. Then, $\Phi_\theta$ and $\Phi_\zeta$ were obtained by solving the contravariant $\theta$ and $\zeta$ components of Eq. (10), thus giving $\vec{\Phi}$, and $A_\theta$ and $A_\zeta$ were obtained similarly to give $\vec{A}$ using the covariant $\theta$ and $\zeta$ components of Eq. (9) with $A_\rho = 0$. Hence, closure of the incompressible full MHD equations involves the solution of five dynamical equations for $\alpha$, $A_\theta$, $A_\zeta$, $\Phi_\theta$, and $\Phi_\zeta$ for a three-dimensional perturbation plus an axisymmetric toroidal equilibrium in the magnetic flux coordinates of the equilibrium. The pressure perturbation does not enter the equations explicitly but can be calculated from the condition $\vec{\nabla} \cdot \vec{v} = 0$. The solution involves a finite difference representation in time and in the radial coordinate $\rho$, and Fourier series expansion is used in $\theta$ and $\zeta$ (for further details, see Refs. 13 and 14). For optimal numerical stability, the linear terms are advanced in time using a fully implicit technique, but the nonlinear terms are evaluated explicitly.

## 3. LINEAR STABILITY

Before discussing the nonlinear properties of the $m = 1$ instability associated with hollow and very flat profiles, it is important to analyze some of its linear properties. The linear stability properties for such profiles have been considered in the past in the large aspect ratio limit,[16,17] and some stability results for low-aspect-ratio tokamaks were presented in Ref. 1. Here, those studies are expanded in some aspects that are important for the understanding of their nonlinear dynamics and also to incorporate shaping effects. Although the following linear studies involve ideal instabilities, the numerical calculations were carried out using $S = 10^7$ for the hollow profiles and $S = 10^5$ for the low-shear

profiles. Comparison with converged ideal growth rates for several cases indicates that the resistivities used do not significantly affect the results.

In Ref. 1 it was shown that the $m = 1$ mode dispersion relation for the case of hollow $q$ profiles and circular cross section plasmas is

$$\bar{\gamma}^{2/3}\left(\bar{\gamma}+\delta q\right)^{1/3} = \frac{1}{\left(\rho_{\min}^2 q''\right)^{1/3}}\left(-\pi\epsilon^2\rho_{\min}^2\delta W_T\right)^{2/3}, \tag{12}$$

where $\bar{\gamma}^2 = 3(\gamma\tau_{H_p})^2 + (\delta q)^2$, $\delta q = q_{\min} - 1$, and $\gamma$ is the linear growth rate. The general expression for $\delta W_T$ up to fourth order in $\epsilon$ is given in Ref. 1 and contains the contribution to $\delta W$ from the $m = 0$ and 2 components. For the particular $q$ profile given in Eq. (3) at $\beta = 0$ and for both $\delta q \ll 1$ and $\Delta q \ll 1$, but large enough for the fourth-order $\delta W$ to dominate over the sixth-order contribution, one has

$$\delta W_T = -\frac{\delta q}{4} - \frac{13}{96}\Delta q. \tag{13}$$

The dispersion relation in this case is

$$\bar{\gamma}^{2/3}\left(\bar{\gamma}+\delta q\right)^{1/3} = \left(\frac{\pi^2}{128}\right)^{1/3}\left(\rho_{\min}\epsilon\right)^{4/3}\frac{\left(\delta q + \frac{13}{24}\Delta q\right)^{2/3}}{\Delta q^{1/3}}. \tag{14}$$

In particular, for $\delta q = 0$ (i.e., for $q_{\min} = 1$), the dispersion relation simplifies further,

$$\gamma\ \tau_{\mathrm{H_p}} \cong 0.163\left(\rho_{\min}\epsilon\right)^{4/3}\left(\Delta q\right)^{1/3}, \tag{15}$$

showing the destabilizing effects of increasing toroidicity ($\epsilon$) and the hollowness ($\Delta q$) of the profile. The stability threshold in $\delta q$ for $\Delta q$ fixed is not given by changing the sign of $\delta W_T$ but by the increased field line bending. Therefore, the linear growth rate does not directly give a measure of the free energy available for the instability to grow. This is an important consideration when analyzing the nonlinear behavior of this mode. From Eq. (14) we can obtain a specific expression for this threshold value, $\delta q = \delta q_c$,

$$\delta q_c = 0.426\ (\rho_{\min}\epsilon)^{4/3}\ \frac{(\delta q_c + \frac{13}{24}\Delta q)^{2/3}}{\Delta q^{1/3}}. \tag{16}$$

Results were shown in Ref. 1 for hollow safety factor profiles with $\Delta q = 0.1$ and $\rho_{\min} = 0.5$. The calculations were carried out with $\beta = 0$ and inverse aspect ratios in the range $0 < \epsilon \leq 0.4$ for varying $q_{\min}$. The numerical results show a sharp onset of ideal instability at $\delta q = \delta q_c$ with $\delta q_c$ small and positive in agreement with Eq. (16). For $q_{\min} > 1 + \delta q_c$ the plasma is ideally stable, while for $q_{\min} < 1 + \delta q_c$ the plasma is unstable with growth rates rising sharply as $q_{min}$ is reduced below the stability boundary. For $\Delta q = 0.1$, these ideal growth rates peak in the vicinity of $q_{\min} \cong 1$. For $q_{\min} \geq 1$, the mode is ideally unstable and resistivity effects are very weak, so that even lowering $S$ to $10^5$ has practically no effect on the structure of the mode and its growth rates. Structurally the mode is an ideal $m = 1$ dominated, $n = 1$ internal kink with a large displacement vector in the plasma core (i.e., for $\rho \leq \rho_{\min}$). The numerical calculations show very good agreement with the analytic results of Eq. (14), exhibiting the $\epsilon^{4/3}$ scaling even down to values of $\epsilon \simeq 0.4$. We have also studied numerically, for circular cross section plasmas having $q_{\min} = 1.0$ and $\rho_{\min} = 0.5$, the dependence of the linear growth rate on the parameter $\Delta q$. In addition, some more general parameterizations, designed to fix the value $q_a = 1.9$ and affecting the $q$ profile only for $\rho > \rho_{\min}$, were used, but the growth rates were insensitive to the changes associated with them. The dispersion relation, Eq. (15), shows that the linear growth rate should be proportional to $(\Delta q)^{1/3}$. Figure 2 plots the $n = 1$ linear growth rate as a function of $(\Delta q)^{1/3}$ for a sequence of hollow profile equilibria with $\Delta q$ varying from 0.0005 to 0.5; the linear relationship between $\gamma$ and $(\Delta q)^{1/3}$ is observed to be satisfied throughout this range. It is interesting to observe how well the large aspect ratio analytic calculations are satisfied in this tight aspect ratio ($\epsilon = 0.4$) regime.

Behavior of the numerically calculated growth rates as a function of $\delta q$ for fixed values of $\Delta q = 0.1$ and 0.01 is compared with that predicted by the dispersion relation, Eq. (14), in Fig. 3. For $\delta q = 0$ ($q_{\min} = 1.0$), the numerical and analytic expressions agree quite

closely. For $\delta q > 0$, the analytic and numerical calculations both lead to similar qualitative behavior. Quantitatively, however, the curves differ for increasing $\delta q$. For values of $\Delta q$ less than 0.01, the discrepancy increases, but for low shear, the fourth-order term in $\delta W$ is no longer dominant, and it is necessary to retain sixth order in the expansion. The quantitative differences between the analytic and numerical growth rate calculations here are not surprising because the analytic results are based on an $\epsilon \ll 1$ expansion, and here $\epsilon = 0.4$ is used. At large aspect ratio ($\epsilon = 0.1$ for example), close quantitative agreement is obtained for all $\delta q$.[1]

The effect of plasma pressure on the $n = 1$ kink mode is shown for the hollow and low-shear profiles in Fig. 4. Both cases were calculated using a circular cross section with $\epsilon = 0.4$ and the pressure profile of Eq. (2). Equation (3) was used for the hollow profile with $q_{\min} = 1.0$, $\Delta q = 0.1$, and $\rho_{\min} = 0.5$, while Eq. (4) was used for the low-shear profile with $\Delta q_\ell = 0$, $q_0 = 1.0$, $\lambda = 6$, and $\rho_0 = 0.75$. Figure 4 shows that, although the linear growth rates increase with $\beta$ for both $q$ profiles, the basic difference between the stability properties is the instability of the hollow profile equilibria at $\beta = 0$ and the marginal stability of the low-shear profile at $\beta = 0$. For $n > 1$, the modes are found to be stable at $\beta = 0$ for both hollow and low-shear profiles. However, as $\beta$ is increased these higher $n$ modes are destabilized as shown at $\beta_0 = 2\%$ in Fig. 5 for the same equilibria as studied in Fig. 4. For $n \leq 8$, the growth rate curves show a peak and then a leveling off for the low-shear profile, but the hollow profile growth rates show a slow linear increase with $n$. The discontinuity of the curve at $n = 1$ for the hollow profile reflects the different character of that mode, which is unstable at $\beta = 0$. Hence, for both types of $q$ profile, higher $n > 1$ pressure-driven modes are destabilized when $\beta \neq 0$.

Now consider, for varying safety factor profiles, the effect of plasma cross section shape on the stability of the $m = 1$ mode. The method used here will be to study sequences of equilibria of various shapes, with each sequence determined by a single $q(\rho)$ profile. Therefore, because of shape effects, the average current $J(\rho)$ changes within each sequence, and

this brings about changes in both the driving terms and the field line bending. In addition to these changes, noncircularity introduces additional couplings between the poloidal components, and these couplings also affect the stability of the modes. It is important to understand and separate these effects.

To do this, first consider, for the hollow profile [Eq. 3] with $q_{\min} = 1.0$, $\rho_{\min} = 0.5$, and $\Delta q = 0.1$, the effect of elongating the plasma. In the case of no triangularity, $\delta = 0$, Fig. 6a shows the $n = 1$ linear growth rate as a function of the elongation $\kappa$ for a sequence of equilibria having $\beta = 0$. The three curves correspond to fixed $\epsilon_H = 0.4$, fixed $\epsilon = 0.4$, and fixed $\epsilon_H = 0.4$, but they include only three poloidal components in the stability calculation. Although most calculations in this paper are carried out at fixed $\epsilon_H = 0.4$, which will be the case unless stated otherwise, the fixed $\epsilon$ curve was calculated here to illustrate the difference for elongated plasmas. Also, unless stated otherwise, all calculations in this paper are carried out with a sufficient number of poloidal components to give converged growth rates. The purpose of calculating the curve containing only three components [the dominant (1;1) and the toroidally coupled (0;1) and (2;1) sidebands] is to separate the effects of the elongated equilibrium from those of the mode coupling caused by elongation. These latter couplings involve the (1;1) harmonic and the twice-removed (-1;1) and (3;1) sidebands, although, for the low aspect ratio considered, the separation between these effects is less obvious. The three-component curve for fixed $\epsilon_H$ shows that, for this profile, the effect of the changing equilibrium on growth rates is initially a mild destabilization, followed by stabilization as the elongation is increased. The effect of the elongation-induced couplings is stabilizing, as can be seen by comparing the three-component and converged curves for fixed $\epsilon_H$. Note that for all these cases ($q \geq 1$) the coupling effect is opposite that for the internal kink with monotonic $q$ profile and $q < 1$ in the plasma core.[18,19] This procedure has been carried out for cases having $q_{\min} > 1$, and again the elongation-induced couplings are found to be stabilizing. The converged curve shows that, for this particular equilibrium sequence, the overall effect of elongating the plasma is one of stabilization.

Comparing the linear growth rates obtained at fixed $\epsilon$ with those at fixed $\epsilon_H$ shows that, for given elongation, the fixed $\epsilon$ growth rates are smaller than those at fixed $\epsilon_H$. This comparison can be clarified by examining the growth rates for each elongation in terms of the similarly defined aspect ratio because this is the only quantity that differs between the two curves. Figure 6b shows, for each elongation tested, the growth rates from the constant $\epsilon$ and constant $\epsilon_H$ curves plotted versus $\epsilon^{4/3}$ together with lines from the points through the origin. Clearly the difference between the constant $\epsilon$ and constant $\epsilon_H$ curves in Fig. 6 is the $\epsilon^{4/3}$ aspect ratio dependence of the growth rate. Except at $\kappa = 2$, where the growth rates are very small and difficult to calculate accurately, the values of $\gamma/\epsilon^{4/3}$ for the constant $\epsilon$ and constant $\epsilon_H$ curves are found to agree to within 5%, and even at $\kappa = 2$ the agreement is within 20%.

Now consider, for the same hollow profile used before, the effects of triangularity for fixed $\epsilon_H = 0.4$, $\beta = 0$, and $\kappa$ (Fig. 7). The two curves in this figure are for $\kappa = 1.0$ and $\kappa = 1.6$. The $\kappa = 1.0$ curve shows, in qualitative agreement with analytical calculations, that triangularity destabilizes the internal kink for these hollow profiles. For $\kappa = 1.6$ the effect is also destabilizing and is stronger than the effect for $\kappa = 1.0$. Indeed, this effect is strong enough to overcome the stabilizing effect of ellipticity. Thus, if $\kappa$ and $\delta$ are varied simultaneously to go from a circular shape to one having $\kappa = 1.6$ and $\delta = 0.3$, the overall effect is destabilizing rather than stabilizing.

The destabilizing effect of triangularity comes mostly from its effect on the equilibrium. To illustrate this result, we have plotted in Fig. 8a the $n = 1$ linear growth rate versus the number of poloidal components used in the calculation for the hollow profile for three different plasma shapes: a circle ($\kappa = 1.0$, $\delta = 0$), a triangular case without elongation ($\kappa = 1.0$, $\delta = 0.5$), and a triangular case with elongation ($\kappa = 1.6$, $\delta = 0.3$). In all three cases, a much stronger growth rate is obtained by using three components, (0;1), (1;1), and (2;1), rather than a single one (1;1). Because (0;1) and (2;1) provide the basic toroidal coupling to (1;1), this shows the necessity of treating these cases properly in toroidal geometry by

including the necessary toroidal couplings. The five-component results include elongation-induced couplings [(-1;1) and (3;1)] in addition to the basic toroidal coupling, and these are seen to be stabilizing. The greatest stabilization is obtained for the elongated case, $\kappa = 1.6$, while the $\kappa = 1$ cases are only slightly affected. In passing to seven components, the triangularity-induced couplings [(-2;1) and (4;1)] to the (1;1) mode are introduced, and these dynamical couplings are seen to be very slightly destabilizing for the cases with $\delta \neq 0$. In all three cases, these seven-component results are essentially converged. For nonelongated plasmas, the three-component growth rates are within 5% of the converged values, and the dynamical effects of the additional shape-dependent couplings are slight. For elongated plasma, the elongation-induced coupling is significantly stabilizing, but in all cases the triangularity-induced couplings show only a slight destabilizing effect. Hence, the overall destabilization caused by triangular plasma shaping, which was observed in Fig. 7, is mainly an effect of the equilibrium properties.

At this point it is useful to introduce some energy-like quantities, which are defined as follows:

$$E^{\mathrm{v}} = \sum_{\substack{(m;n) \\ \neq (0;0)}} \left( E^{\Phi_\theta}_{(m;n)} + E^{\Phi_\zeta}_{(m;n)} \right) \tag{17}$$

and

$$E^{B} = \sum_{\substack{(m;n) \\ \neq (0;0)}} \left( E^{A_\theta}_{(m;n)} + E^{A_\zeta}_{(m;n)} \right) , \tag{18}$$

where, for any field $f$,

$$E^{f}_{(m;n)} = \int \left[ \left( \frac{\partial f_{(m;n)}}{\partial \rho} \right)^2 + \left( \frac{1}{\rho} \frac{\partial f_{(m;n)}}{\partial \theta} \right)^2 \right] d\tau \ , \tag{19}$$

with the summations taken over all components except (m;n) = (0;0) and the volume integration taken over the entire plasma. Figure 8b plots the magnetic field norms

$E^B_{(m;n=1)} = E^{A_\theta}_{(m;n=1)} + E^{A_\zeta}_{(m;n=1)}$ versus $m$ for the eigenfunctions of the three cases considered in Fig. 8a. The structure of these plots clearly shows the effects of cross section shape. In particular, the norms for the circular cross section case decay monotonically moving away from $m = 1$. The elongated case shows secondary peaks at $m = -1$ and $m = 3$; for the triangular case, secondary peaks occur at $m = -2$ and $m = 4$. It is interesting that similar plots of the velocity norms $E^v_{(m;n)} = E^{\Phi_\theta}_{(m;n)} + E^{\Phi_\zeta}_{(m;n)}$ show little effect of changing the cross section shape. For all three cases, the values decay monotonically away from the peak at $m = 1$, and the results for the three curves are in close agreement.

We now study for several shapes the behavior of linear growth rate as a function of $q_{\min}$ with the safety factor profile otherwise fixed as above with $\Delta q = 0.1$ and $\rho_{\min} = 0.5$ in Eq. (3). Figure 9 shows this dependence for plasmas having $\delta = 0$ and $\kappa = 1.0, 1.4, 1.6$ and 2.0 as well as for $\kappa = 1.6$, $\delta = 0.3$. Figures 6a ($\epsilon_H = 0.4$) and 7 give the $q_{\min} = 1.0$ results shown here. Note that, as $q_{\min}$ is increased above 1.0, the growth rate achieves a maximum value, except for the circular cross section case for which the maximum is at $q_{\min}$ somewhat less than 1.0. The maximum growth rate is quite close to the value obtained at $q_{\min} = 1.0$, and for further increases in $q_{\min}$, the growth rate drops at first gradually and then quite sharply near the stability boundary. For these cases, larger values of $q_{\min}$ at the stability boundary correspond to larger growth rates at $q_{\min} = 1.0$ (i.e., the curves are enveloped and do not cross). Hence, for several shapes, including elongation and triangularity, the dependence of the linear $n = 1$ growth rates for the ideal internal kink as a function of $q_{\min}$ is similar to that found earlier[1] for a circular cross section displaying, in particular, a very sharp stability boundary. It is also important to note that changes in shape can produce sudden onset of the instability. Figure 9 shows that decreasing the elongation or increasing the triangularity for fixed profile with $q_{\min} > 1$ can change the plasma from stable to unstable.

As for the stability of the zero-shear profiles, some results were presented in Ref. 1 for the $q$ profile given in Eq. (4). In that paper, $\Delta q_\ell = 0$, $\lambda = 6$, and $\rho_0 = 0.462$ (we use

$\rho_0 = 0.75$ here) were used for circular cross section plasmas with varying $q_0$ and $\beta$. In this case, the ideal $n = 1$ linear eigenfunctions are pressure driven and stable at $\beta = 0$ for $q_0$ above 1. The stability is marginal at $q_0 = 1$, and as $\beta$ is increased an unstable ideal mode is found. This is shown in Fig. 4, which contrasts the $\beta$ dependence of the $n = 1$ linear growth rates for the low-shear and hollow profiles. As with the hollow profile, the finite $\beta$ mode demonstrates a sharp stability boundary at $q_0 = 1 + \delta q_c$ for $q_0$ slightly above unity. Below this value is an $n = 1$ instability. For $q_0 \geq 1$, the growth rate and structure of the mode are fairly independent of resistivity, and the mode is ideally unstable. Structurally the mode is $m = 1$ dominated with a large displacement vector in the plasma core; Wesson refers to this instability as a quasi-interchange mode.[9]

We have studied, for these essentially shearless profiles, the effects of shaping and profile variation. The results presented here were calculated at inverse aspect ratio $\epsilon_H = 0.4$ and peak plasma beta $\beta_0 = 2\%$. The pressure profile of Eq. (2) was used together with the safety factor profile of Eq. (4) with $\Delta q_\ell = 0$, $\lambda = 6$, and $\rho_0 = 0.75$. In Fig. (10a) the $n = 1$ linear growth rates are plotted as functions of $q_0$ for shaped plasmas having no triangularity, $\delta = 0$, and elongation $\kappa = 1.0$, 1.2, 1.4, and 1.6. Note that in all cases the growth rate curves peak at some value of $q_0 > 1$ and then decrease to zero at somewhat larger $q_0$. The effect of the elongation is to shift the peak and upper stability boundary to higher values of $q_0$. Values of the peak growth rates at first increase and then decrease with increasing elongation. An analysis of the couplings in terms of components shows behavior similar to that observed for hollow profiles in Fig. 8. The addition of the (-1;1) and (3;1) components, which are coupled to the (1;1) by elongation effects, reduces the linear growth rate significantly from that obtained using three components. A combination of these stabilizing couplings and the effects of the elongated equilibrium determines the overall effect on the stability of the mode. Figure 10b shows that adding triangularity to the plasma cross section destabilizes the $n = 1$ mode, both for circular and elongated plasmas. As for the hollow profiles, this destabilization can be shown to be caused by the

change of equilibrium. The addition of the triangularity-coupled (-2;1) and (4;1) modes has little effect on growth rates, which are essentially converged using five components; thus, the triangularity-induced couplings have little influence.

The effects of cross section elongation on the $n = 1$ mode are contrasted for the hollow and low-shear profiles in Fig. 11. The parameterizations of Eqs. (3) and (4) were used with $\Delta q = 0.1$ and $\rho_{\min} = 0.5$ in Eq. (3) and $\lambda = 6$, $\rho_0 = 0.75$, and $\Delta q_\ell = 0$ in Eq. (4). The cases shown were for no triangularity, $\delta = 0$, and horizontal inverse aspect ratio $\epsilon_H = 0.4$. For the hollow profile cases, increasing either $q_{\min}$ or the elongation, $\kappa$, tends to stabilize the mode. These instabilities were calculated for equilibrium values of $\beta = 0$. For the low-shear equilibria, $\beta_0 = 2\%$ was chosen. In these cases, elongating the plasma at first destabilizes the mode, leading to a peak in the growth rate curve beyond which further elongation stabilizes the mode. Increasing the value of $q_0$ leads to different curves for which the instability is transferred to higher elongations. Hence, the effects of elongation on these two types of instability are basically different.

The sensitivity of the linear stability, the driving forces, and the growth rates of the $n = 1$ mode to small changes in the safety factor profile should be apparent. As a final illustration of this sensitivity, consider the transition from very low shear to hollow safety factor profile given by varying $q_0$ and $\Delta q_\ell$ in Eq. (4) with fixed $\lambda = 6$, $\rho_0 = 0.75$, $\rho_{\min} = 0.5$, and $\Delta\rho = 0.1$. These parameters superimpose on the low-shear profile just discussed a local minimum of depth $\Delta q_\ell$ and width $\Delta\rho$ centered at $\rho_{\min}$, and for $\Delta q_\ell = 0$ the low-shear profile is obtained. For $q_0 = 1.1$ and $\Delta q_\ell = 0.1$, this profile is compared with the hollow and very low shear profiles in Fig. 1. For these calculations, we choose $\epsilon_H = 0.4$ and $\beta_0 = 0$ and 2% as above and a plasma shape ($\kappa = 1.6$, $\delta = 0.3$). The linear stability results of this study are presented in Fig. 12. Figure 12a shows the $n = 1$ linear growth rate as a function of $q_0$, both with $\Delta q_\ell = 0$ (no local minimum) and with $\Delta q_\ell = q_0 - 1$ (a local minimum of $q_{\min} \approx 1$). For the flat profile without local minimum, the result at $\beta_0 = 2\%$ is as shown in Fig. 10b, with a stability boundary at $q_0 = 1.03$ and a peak growth rate at $q_0 = 1.015$. At

$\beta_0 = 0$, this pressure-driven mode is stable. Although the linear growth rate at $\beta_0 = 2\%$ is not extremely different for the hollow profile when $q_0 \lesssim 1.015$, for values above this the hollow profile becomes increasingly unstable, while the low-shear profile is stabilized. Hence, as $q_0$ is increased with $q_{\min} = 1.0$, comparison with the low-shear profile shows that the local hollow nature leads to destabilization. Carrying out the same sequence of calculations for the locally hollow profile with $\beta = 0$ and $q_{\min} = 1.0$ shows an increase in linear growth rate from marginal at $q_0 = 1$ as $q_0$ increases. To further illustrate this sensitivity, Fig. 12b plots the $n = 1$ linear growth rate as a function of $q_{\min} \approx q_0 - \Delta q_\ell$ for $q_0 = 1.03$ (marginally stable for $\Delta q_\ell = 0$) and $q_0 = 1.04$. Both cases become unstable, with similar rapidly increasing growth rate curves, as $q_{\min}$ is decreased below the boundary at 1.03. Hence, small local changes in the safety factor profile can trigger robust ideal $n = 1$ instabilities with linear growth rates around $10^{-2}\tau_{H_p}^{-1}$.

## 4. NONLINEAR EVOLUTION OF THE INTERNAL KINK

To understand the dynamics of the internal kink evolution, numerical calculations have been carried out for a variety of profiles and plasma shapes. To limit the considerations to ideal kinks, only $q$ profiles with $q(\rho) \geq 1$ have been considered. Some of the properties of the nonlinear evolution are common to all profiles and shapes considered. Let us begin by describing the general properties of the nonlinear evolution of the $m = 1$ internal kink mode. Although the calculations studied here involve ideal instabilities, the nonlinear calculations are carried out using $S = 10^5$.

For a general description of the properties of the nonlinear evolution let us consider a case with $q(\rho) > 1$. Figure 13 shows the evolution of the velocity norm for a small initial perturbation of an equilibrium having $\epsilon_H = 0.4$, $\beta_0 = 2\%$, $\kappa = 1.6$, $\delta = 0.3$, and a safety factor given by Eq. (4) with $\Delta q_\ell = 0$, $q_0 = 1.015$, $\rho_0 = 0.75$, and $\lambda = 6$. The linear growth rate for this case is $\gamma \approx 10^{-2}\tau_{H_p}^{-1}$. The time scale for the evolution is essentially $\gamma^{-1}$ for $t \lesssim 400\tau_{H_p}$, as can be seen from the exponential growth of $E^v$ with an $e$-folding

time of about $50\tau_{H_p}$. After $400\tau_{H_p}$ nonlinear effects lead to a saturation of the instability, with $E^v$ peaking at $t = 600\tau_{H_p}$. Figure 14 shows vector plots of the velocity in the $\zeta = 0$ plane, which reveal a dominant $m = 1$ convective motion throughout the plasma core. Because the instability is ideal and evolving rapidly, we expect the magnetic field to be carried by the convective motion illustrated here. The times of the plots are indicated by the arrows in Fig. 13. The initial plot, taken at $t = 600\tau_{H_p}$, shows a convective motion, which, in this plane, should transport the central plasma and magnetic field to the right. Subsequent plots at $t = 752\tau_{H_p}$ and $t = 947\tau_{H_p}$, when taken together with the velocity norm of Fig. 13, show the saturation, decrease, and reversal with smaller amplitude of this motion. Figure 15 illustrates the effect of the instability on the magnetic field configuration by plotting the magnetic surfaces in the $\zeta = 0$ plane. At $t = 600\tau_{H_p}$, the time of peak saturation of the instability, the plasma core has been shifted to the right (for $\zeta = 0$) by the convective motion, shown in Fig. 14. In comparison with equilibrium, the magnetic axis has been shifted $x = 0.25$ to the right on the horizontal scale. The subsequent field line plots at $752\tau_{H_p}$ and $947\tau_{H_p}$ show no further change in the shift of the magnetic axis, a behavior in keeping with the saturation of the instability, which will be examined in detail later. However, the shape of the shifted core continues to change in response to the velocity field of the instability, becoming somewhat more crescent shaped at later times. Although the shift generated by the instability is shown to be outward in the $\zeta = 0$ plane (Fig. 15), the $m/n = 1/1$ helical nature of the instability is manifested by examining the magnetic surfaces in several poloidal planes (Fig. 16). The plots in Fig. 16 were taken from a different case having a hollow profile and $q_{\min} = 1.0$, which leads to the magnetic bubble to be discussed later, but the $m/n = 1/1$ helical behavior is quite general to all these cases. The total evolution is governed by ideal MHD, as is the time scale, and the magnetic field line topology remains unchanged.

Let us now consider two cases in which $q \geq 1$, with $q = 1$ at one radial position. As a first example, we take the case of a hollow $q$ profile with $q_{\min} = 1$. Figure 17 shows

the magnetic field line plots at four different times for the evolution of a small initial perturbation of a circular cross section equilibrium with $\epsilon_H = 0.4$, $\beta = 0$, and the $q$ profile parameters $\Delta q = 0.1$, $\rho_{\min} = 0.5$, and $q_{\min} = 1.0$ in Eq. (3). The nonlinear evolution of the instability is consistent with the one given earlier, but now an additional topological feature is caused by the presence of a $q = 1$ surface. The initial perturbation of the equilibrium has changed the topology such that a new magnetic axis appears close to the $q = 1$ surface. The new magnetic surface structure is different than the one created by a tearing mode. The nonlinear evolution does not resemble the growth of a magnetic island but is more reminiscent of the nonlinear evolution of a vacuum magnetic bubble.[20] Although other aspects of the evolution, particularly the shift and subsequent crescent shaping of the core because of the $m = 1$ convective motion, are unaffected by the presence of the magnetic bubble, the details of the evolution pertaining to the bubble could be affected by the value of $S$.

Another special case occurs when $q$ is very close to unity throughout most of the plasma core. Such cases include the low-shear profiles when $q_0 \approx 1$ and also the hollow profiles when $\Delta q \ll 1$. Consider, for example, the case depicted by the field line plots in Fig. 18. In this example, the low-shear $q$ profile of Eq. (4) is used with $\Delta q_\ell = 0$, $q_0 = 1.0$, $\rho_0 = 0.75$, and $\lambda = 6$ for a circular cross section plasma having $\epsilon_H = 0.4$ and $\beta_0 = 2\%$. For this profile, the rate of increase in $q$ throughout the plasma core is so slow that $q$ changes from 1.0 at $\rho = 0$ to 1.0013 at $\rho = 0.5$. Figure 18 shows that the penetration of the outside plasma into the center is more pronounced for this case, as is the crescent formation by the shifted plasma core, than for cases having larger $q$ through most of the core. In this case, the plasma core is essentially a large $q = 1$ region. The high $n$ modes, which are linearly unstable for this case, play a more important role, and distortion of the magnetic surfaces is characterized by $m$ modes higher than $m = 1$. Despite the existence of unstable high $n$ modes of the 1/1 helicity, we have observed no nonlinear acceleration effects in any of the cases studied.

Let us now consider some systematics of the evolution. We focus on a sequence of equilibria having $\epsilon_H = 0.4$, a circular cross section, $\beta = 0$, and a hollow $q$ profile ($\rho_{\min} = 0.5$, $\Delta q = 0.1$) with $q_{\min}$ varying between 1.0 and 1.02. The linear growth rates for this sequence are plotted in Fig. 9 ($\kappa = 1.0$, $\delta = 0$ curve). They reach a maximum for $q_{\min} = 1.0$, and the marginal stability equilibrium is at $q_{\min} = 1.018$. The saturation level of the instability-induced flow velocity increases as $q_{\min}$ goes from 1.015 to 1.0. This is shown in Fig. 19a, where the velocity norm is plotted as a function of time for several values of $q_{\min}$; in all cases, near exponential growth is followed by saturation. As saturation is reached, the 1/1 component of the velocity reverses. This can be seen in Fig. 19b, where the maximum of the (1;1) component of $\Phi_\theta$ (the $\theta$ component of the velocity stream vector) is plotted versus time for each of the cases considered. The curves have been shifted in time in Fig. 19b to give equal initial values of $\Phi_\theta^{\max}$. The peaks in $\Phi_\theta^{\max}$ correspond closely in time to those for $E^v$ in Fig. 19a. The magnetic axis shifts as the instability grows, as shown in Fig. 17 for the particular case with $q_{\min} = 1.0$. The saturation of the axis shift is simultaneous with the velocity reversal, as should be expected for an ideal instability. Figure 20 shows this result for the case of $q_{\min} = 1.0$. The saturated axis shift decreases as $q_{\min}$ increases toward the marginal stability point $q_{\min} = 1.018$. Figure 21 shows the corresponding magnetic field line plots of the saturated instabilities for the four values of $q_{\min}$; note that the shifts decrease as $q_{\min}$ increases toward the stability boundary. The value of the magnetic axis shift is correlated with the total fluid displacement. To estimate this displacement, we multiply the peak value of $\Phi_\theta^{\max}$ by $1/\gamma_{n=1}$, the inverse of the $n = 1$ linear growth rate for each case (Fig. 9), which is proportional to the time over which the instability acts. The correlation between the magnetic axis shift and $\Phi_\theta^{\max}/\gamma_{n=1}$ is shown in Fig. 22. After saturation, $\Phi_\theta^{\max}$ changes abruptly (Fig. 20), changing its sign in the process, so that the flows are reversed. This change in velocity flow behavior can also be seen in the velocity vector plots (Fig. 14), and it is responsible for the change in the shape of the flux surfaces, which increase their crescent shape after saturation.

In concluding this section, we note that the effects of cross section shaping and plasma $\beta$ are less pronounced than the sharp sensitivity to profile variations. Even at $\beta = 0$, where the low-shear profiles are linearly stable, very slight local changes can hollow such profiles and lead to destabilization. Neither changes in plasma pressure nor variations in cross section shape have been found to significantly affect the earlier description of the nonlinear evolution of the $m = 1$ instability. For example, the case considered in Figs. 13–15 was calculated for an equilibrium having $\kappa = 1.6$, $\delta = 0.3$, and $q_0 = 1.015$ in Eq. (4) which falls at the peak of the corresponding linear growth rate curve in Fig. 10b. Calculations for circular cross section, made at $q_0 = 1.005$ or 1.01 to fall well within the unstable region of the corresponding mode, evolve in keeping with the earlier description. The hollow profile cases shown in Figs. 16 and 17 differ only in the shape of the plasma cross section, and again in both cases the evolution fits the earlier description including the magnetic axis shift, saturation, and magnetic bubble formation. Calculations like that depicted in Fig. 17, but at $\beta \neq 0$, show this same process. Although details such as time scales (which are dependent on the values of linear growth rate), saturation levels of the norms, or the exact parameter values for the profiles differ with $\beta$ and cross section shape, the overall description of the nonlinear process is not crucially shape or, for hollow $q$, $\beta$ dependent.

## 5. NUMERICAL CONSIDERATIONS

References 13 and 14 discuss the numerical scheme used in these calculations, and other publications have considered some of the problems regarding numerical convergence of the nonlinear calculations.[21–24] The particular calculations presented here are rather benign, in that they are almost single-helicity dominated. However, we will now discuss the numerical aspects of the calculations that are directly relevant to the results of Sect. 4.

Although the nonlinear process described in this section is dominated by ideal MHD, the numerical calculations include explicit dissipation terms, apart from the dissipation

induced by a finite-size grid. In particular, resistivity is nonzero and a value of $S = 10^5$ is included. As stated before, for profiles with $q \geq 1$ the resistivity has little effect on the linear structure and growth rates of these ideal instabilities. Typically, at $S = 10^5$ the linear growth rates are within a few percent of the ideal values and the eigenfunctions are visibly indistinguishable from the ideal ones. Nonlinearly, it is therefore expected that the observed evolution will be ideally determined, with the value of the resistivity affecting only the long-term behavior through reconnection. By repeating some of the nonlinear calculations with different values of $S$, we have confirmed the independence of the dynamics of the nonlinear evolution from the resistivity.

For numerical stability of the nonlinear evolution, we have also found it necessary to include a small ion viscosity in the momentum equation. Typically a constant value of $\nu/S = 10^{-6}$, which is small enough not to affect the linear growth rates, is used. Numerical tests, using different values of the viscosity in repeating nonlinear calculations, have been performed. As with the resistivity tests, the independence of the dynamical evolution from the viscosity has been demonstrated.

For low-shear profiles at nonzero $\beta$ values, some of the high $n$ modes are linearly unstable (Fig. 5), and they have a visible effect on the nonlinear evolution of the flux surfaces (Fig. 18). Therefore, it is important to discuss the mode spectrum used in the nonlinear calculations. The mode selection we have used for most of the nonlinear calculations includes 32 components: $(m = -2 \rightarrow 4;\ n = 1)$, $(m = 0 \rightarrow 4;\ n = 2)$, $(m = 2 \rightarrow 5;\ n = 3)$, $(m = 3 \rightarrow 5;\ n = 4)$, $(m = 4 \rightarrow 6;\ n = 5)$, $(m = 6;\ n = 6)$, $(m = 7;\ n = 7)$, and $(m = 0 \rightarrow 7;\ n = 0)$. To assess the effect of these higher $n$ modes on the nonlinear evolution, the calculation for the case shown in Fig. 18 was carried out both for the usual 32-mode set defined above and for 44 modes in which the (1;3), (2;4), (6;4), (3;5), (7;5), (4;6), (5;6), (7;6), (8;6), (6;7), (8;7), and (8;8) components were added. The evolution of the overall velocity norm $E^{\mathrm{v}}$ for both calculations is shown in Fig. 23 together with that of $E^{\mathrm{v}}_{(5;5)}$ and $E^{\mathrm{v}}_{(6;6)}$ from the 44-mode calculation. It is apparent that up through and beyond

the saturation the two calculations are in good agreement and that $E^{V}_{(5;5)}$ and $E^{V}_{(6;6)}$ remain small. Figure 24 plots the spectra of the velocity norms at $t = 1100\tau_{H_p}$ (saturation) and $1350\tau_{H_p}$. The results at $1100\tau_{H_p}$ show close agreement up to about $n = 5$, at and above which the 44-mode results are larger than those obtained using 32 modes. For $n = 6$ and $n = 7$, this is probably caused by inclusion of the toroidal curvature effects through the couplings to the satellite modes. As seen earlier for $n = 1$ (Fig. 8a), these couplings enhance the linear growth rates. We also note that the magnitudes of these high $n$ velocity norms are small, in both cases, compared with those for lower $n$, and that for each $n$ the peak is in the 1/1 helicity; therefore, in addition to the linear growth for each $n$ mode, nonlinear driving from other $n$ modes is significant, particularly in the 1/1 helicity. Figure 24b, taken at $1350\tau_{H_p}$, shows greater differences between the two calculations, with the first occurrence at $n = 2$. For both calculations, especially the 32-mode case, the higher $n$ velocity spectra have become flat, and a higher number of modes would be necessary to represent well the long-time behavior. However, the $n = 1$ peaks and the overall velocity norms are still in reasonable agreement for both cases, so that the differences in the high $n$ evolution for the two cases have not significantly affected the global evolution (i.e., shift) at this time, nor has the overall saturation level been affected. An analysis of the mode spectrum for a hollow profile case at $\beta = 0$ [using a more general parameterization described in Eq. (22)] indicates that 32 components are sufficient to describe the evolution to saturation ($t = 1300\tau_{H_p}$), during which the $n = 1$ mode is dominant (Fig. 25a). At later times ($t = 1600\tau_{H_p}$), however, the $n = 1$ velocity norm decreases while the higher $n$ modes increase, thus flattening the spectrum (Fig. 25b); to consider the detailed evolution at these later times would require additional modes.

## 6. DISCUSSION

The nonlinear calculations show that the saturated axis shift does not correlate with the linear growth rate, which is not surprising. The saturation axis shift will depend on the

mechanism of nonlinear saturation. In this particular case, it seems that the mechanism is the increased field line bending generated by the shift of the plasma. In the equilibrium flux coordinate system, the nonlinear evolution changes the profile by an amount $(\widetilde{\delta q})$. This change has to be such that in the flux coordinate system of the final state the $q$ profile has not changed (the nonlinear evolution is ideal). This gives the relation

$$\frac{\Delta}{a} \approx \sqrt{\frac{16(\widetilde{\delta q})}{q''}}. \tag{20}$$

At saturation, $(\widetilde{\delta q})$ has to be equal to the change of $q$ required to stabilize the mode; that is, for the hollow $q$ profile, $(\widetilde{\delta q}) = \delta q_c - \delta q$. For the hollow $q$ profile given by Eq. (3), this implies

$$\frac{\Delta}{a} \approx \rho_{\min} \sqrt{2\frac{\delta q_c - \delta q}{\Delta q}}\,. \tag{21}$$

An analytic calculation of the saturated displacement[25] gives the result

$$\left(\frac{\Delta}{a}\right)^2 \frac{q''}{\delta q} = \frac{8}{71}\left(\frac{8\pi}{3}\right)^2 \left[\left(\frac{\delta q_c}{\partial q}\right)^{3/2} - 1\right] \tag{22}$$

in the limit $(\delta q_c - \delta q)/\delta q < 1$. In this calculation the nonlinear field line bending effects are found to be more important within the layer at $q_{\min}$ than elsewhere. The helical equilibrium equation is solved in the layer (subject to accessibility conditions) and matched to the outer regions on either side. Equation (22) agrees in form with Eq. (20) and, because the calculation of Ref. 25 is asymptotically rigorous, shows that the numerical constant inside the square root is 11.86.

In Fig. 26, the saturated axis shift has been plotted versus $(\delta q_c - \delta q)$ for several of the cases studied. First consider the sequence of hollow profile equilibria, which were discussed in detail in Sect. 4 (Figs. 18–22). The predicted shift for this sequence (for which $\Delta q = 0.1$ and $\delta q_c = 0.018$) is given according to Eq. (20) by a solid straight line and according to Eq. (22) by the dashed curve in Fig. 26. Both analytic expressions are found to agree

reasonably well with each other and with the results of the numerical calculations. Also shown on Fig. 26 are the equivalent data for two cases having the same $q$ profile, $\epsilon_H = 0.4$ and $\beta = 0$, but with elongation $\kappa = 1.6$ and triangularity $\delta = 0.3$. Figure 9 shows that for this cross-sectional shape, $\delta q_c = 0.027$, and the two cases shown have $\delta q = 0$ and 0.01. Estimates of the shift and the minor radius for this case are complicated by the noncircularity of the plasma cross sections. For the circular plasma sequence, magnetic field line plots in different poloidal planes show that the magnetic axis describes a circular helical path so that the poloidal projection of this orbit is a circle. For the noncircular cases, this projection is also noncircular, and the plotted points are for the maximum shift normalized to the generalized minor radius. Therefore, the critical parameters for understanding the nonlinear dynamics are the field line bending term and the details of the $q$ profile. The results do not indicate any strong sensitivity to the shaping except that the shaping modifies the equilibrium. In this sense, the inclusion of toroidicity and shaping has qualitatively not changed the conclusions of Refs. 9–11, where the nonlinear calculations were limited to circular cross section cylindrical geometry.

Sensitivity to the $q$ profile provides a potential explanation of the rapid sawtooth crash, which appears on large tokamaks. The crash is called rapid because the observed time for the event is much less than the predicted reconnection time using the Kadomtsev model. For example, on JET the rapid crash takes typically 100 $\mu s$, or about $500\tau_{H_p}$, while the Kadomtsev prediction of 5 ms is a factor of 50 greater than the observed value.[4] The observed crash time of $500\tau_{H_p}$ is commensurate with the nonlinear evolution times of the cases considered in this work, which were calculated using the geometric parameters of JET. Furthermore, it has been experimentally observed,[2] using X-ray tomography, that the hot plasma core is helically shifted and then distorted into a crescent during the crash. This also is consistent with the nonlinear evolution studied here. An important question concerns how this rapid process can be suddenly triggered. This implies that we must have $\delta q_c - \delta q$ such that $\gamma_{n=1}^{-1} \approx 500\tau_{H_p}$, and $\Delta/a \approx 0.2$; given the slow rate of profile change,

$\delta q_c - \delta q$ must be small to be compatible with the fast trigger. By looking at Eqs. (14) and (21), we see that reducing $\Delta q$ could be a way of achieving the types of profiles that could be compatible with experimental data. To do that, we use the more complicated $q$ profile parameterization

$$q(\rho) = \begin{cases} q_{\min} + \Delta q_{\text{in}} \left[1 - \left(\dfrac{\rho}{\rho_{\min}}\right)^2\right]^2 & \text{for } \rho \leq \rho_{\min} \\ q_{\min} + \Delta q_{\text{out}} \left[1 - \left(\dfrac{\rho}{\rho_{\min}}\right)^2\right]^2 & \text{for } \rho \geq \rho_{\min} \end{cases}, \tag{23}$$

which permits the reduction of $q''$ at $\rho_{\min}$ while keeping constant $q = q_a$ at the plasma edge. By choosing $\Delta q_{\text{in}} = 0.003$, the maximum growth rate is $\gamma = 3.87 \times 10^{-3}\ \tau_{H_p}^{-1}$ for $q_{\min} \simeq 1.005$ and the stability threshold is at $\delta q_c = 0.012$. Nonlinearly, the profile with $q_{\min} = 1.005$ gives rise to the previously described evolution with the saturation of the velocity norm and the magnetic axis shift requiring about $1000\tau_{H_p}$. The magnetic field lines are plotted for the saturated state in Fig. 27, and they show the pronounced crescent formation and large magnetic axis shift typical of $q \approx 1$ evolutions. For this family of profiles, reasonable time scales for the sawtooth crash and for the magnitude of the shift can be obtained with $\delta q_c - \delta q \approx 3 \times 10^{-3}$.

## 7. CONCLUSIONS

We have studied the nonlinear evolution of the internal kink in toroidal geometry for shaped cross section plasmas and $q$ profiles such that $q \geq 1$. The results of these studies lead to the following conclusions.

1. Instability grows nonlinearly in the ideal linear time scale, namely several hundred to 1000 poloidal Alfvén times. Magnetic surfaces are not broken by resistive effects on this short time scale.

2. The instability saturates at a finite amplitude, causing a nearly helical shift of the plasma magnetic axis. The plasma displacement deforms the central flux surfaces into a crescent-shaped region and carries outside flux surfaces into the center of the crescent.
3. Shaping effects are relatively weak, but there is strong sensitivity to the $q$ profile and, for low-shear profiles, to $\beta$.
4. The nonlinear saturation mechanism is the increase in the field line bending.
5. Evolution times of $10^3 \tau_{H_p}$ and axis shifts of 20% minor radius can be obtained for changes in $q$ profile of only $3 \times 10^{-3}$ from marginal stability.

These results are consistent with the experimental observations of the fast sawtooth crash process[2] seen on large tokamaks. The numerically and experimentally determined time scales agree, and the calculated displacement of the magnetic surfaces is highly suggestive of the X-ray tomography measurements on JET. Finally, the sudden transition from stability to robust instability with small changes in $q$ is consistent with the rapid trigger of the experimentally observed fast sawtooth.

## REFERENCES


1. R. J. Hastie, T. C. Hender, B. A. Carreras, L. A. Charlton, and J. A. Holmes, Phys. Fluids **30**, 1756 (1987).
2. A. W. Edwards, D. J. Campbell, W. W. Engelhardt, H. U. Fahrbach, R. D. Gill, R. S. Granetz, S. Tsuji, D. J. D. Tubbing, A. Weller, J. Wesson, and D. Zasche, Phys. Rev. Lett. **57**, 210 (1986).
3. B. B. Kadomtsev, Sov. J. Plasma Phys. **1**, 389 (1975).
4. J. A. Wesson, Plasma Phys. Controlled Fusion **28**, 243 (1986).
5. W. Pfeiffer, Nucl. Fusion **25**, 673 (1985).
6. R. E. Denton, J. F. Drake, R. G. Kleva, and D. A. Boyd, Phys. Rev. Lett. **56**, 2477 (1986).
7. K. McCormick et al., in Controlled Fusion and Plasma Physics (Proc. 12th European Conf., Budapest, 1985) Vol. 1, 199.
8. M. N. Bussac, R. Pellat, D. Edery, and J. L. Soule, Phys. Rev. Lett. **35**, 1638 (1975).
9. J. A. Wesson, P. Kirby, and M. F. F. Nave, Eleventh International Conf. on Plasma Physics and Controlled Nuclear Fusion Research (IAEA-CN-47/E-I-1-1, Kyoto, 1986).
10. P. Kirby, Culham Laboratory Preprint CLM-P809 (1987), submitted to Nuclear Fusion.
11. A. Y. Aydemir and R. D. Hazeltine, University of Texas Institute for Fusion Studies Report No. 250 (1986).
12. A. Y. Aydemir, Phys. Rev. Lett. **59**, 649 (1987).
13. L. A. Charlton, J. A. Holmes, H. R. Hicks, V. E. Lynch, and B. A. Carreras, J. Comput. Phys. **63**, 107 (1986).
14. L. A. Charlton, B. A. Carreras, J. A. Holmes, and V. E. Lynch, submitted to Phys. Fluids.
15. J. A. Holmes, Y-K. M. Peng, and S. J. Lynch, J. Comput. Phys. **36**, 35 (1980).
16. A. A. Ware, Phys. Rev. Lett. **26**, 1304 (1971).

17. V. D. Shafranov, Sov. Phys. Techn. Phys. **15**, 175 (1970).

18. D. Edery, G. Laval, R. Pellat, and J. L. Soulé, Phys. Fluids **19**, 260 (1976).

19. J. W. Conner and R. J. Hastie, Culham Laboratory Report CLM-M106 (Culham Laboratory, UKAEA, 1985).

20. R. B. White, D. Monticello, M. N. Rosenbluth, H. Strauss, and B. B. Kadomtsev, in Plasma Physics and Controlled Nuclear Fusion Research 1974, (IAEA, Vienna, 1975) Vol. 1, p. 495.

21. H. R. Hicks, B. A. Carreras, J. A. Holmes, D. K. Lee, and B. V. Waddell, J. Comput. Phys. **44**, 46 (1981).

22. V. E. Lynch, B. A. Carreras, H. R. Hicks, J. A. Holmes, and L. Garcia, Comput. Phys. Commun. **24**, 485 (1981).

23. H. R. Hicks, B. A. Carreras, L. Garcia, and J. A. Holmes, Oak Ridge National Laboratory Report ORNL/TM-9127 (1984).

24. L. Garcia, H. R. Hicks, B. A. Carreras, L. A. Charlton, and J. A. Holmes, J. Comput. Phys. **65**, 253 (1986).

25. Avinash, R. J. Hastie, J. B. Taylor, and S. C. Cowley, submitted to Phys. Rev. Lett.

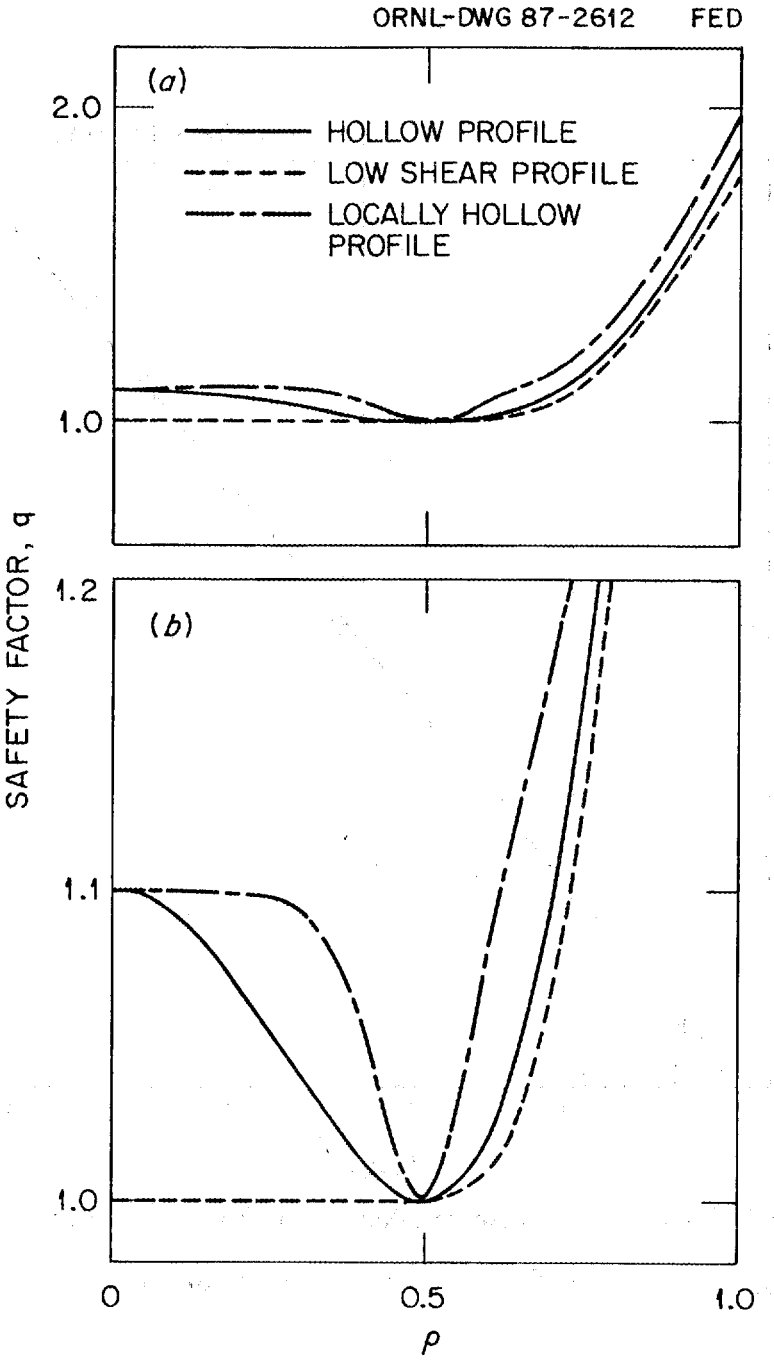


Fig. 1. Examples of safety factor profiles, given by Eqs. (3) and (4), which are subject to internal kink instability. Plots on two scales emphasize (a) global similarities and (b) detailed differences in plasma core.

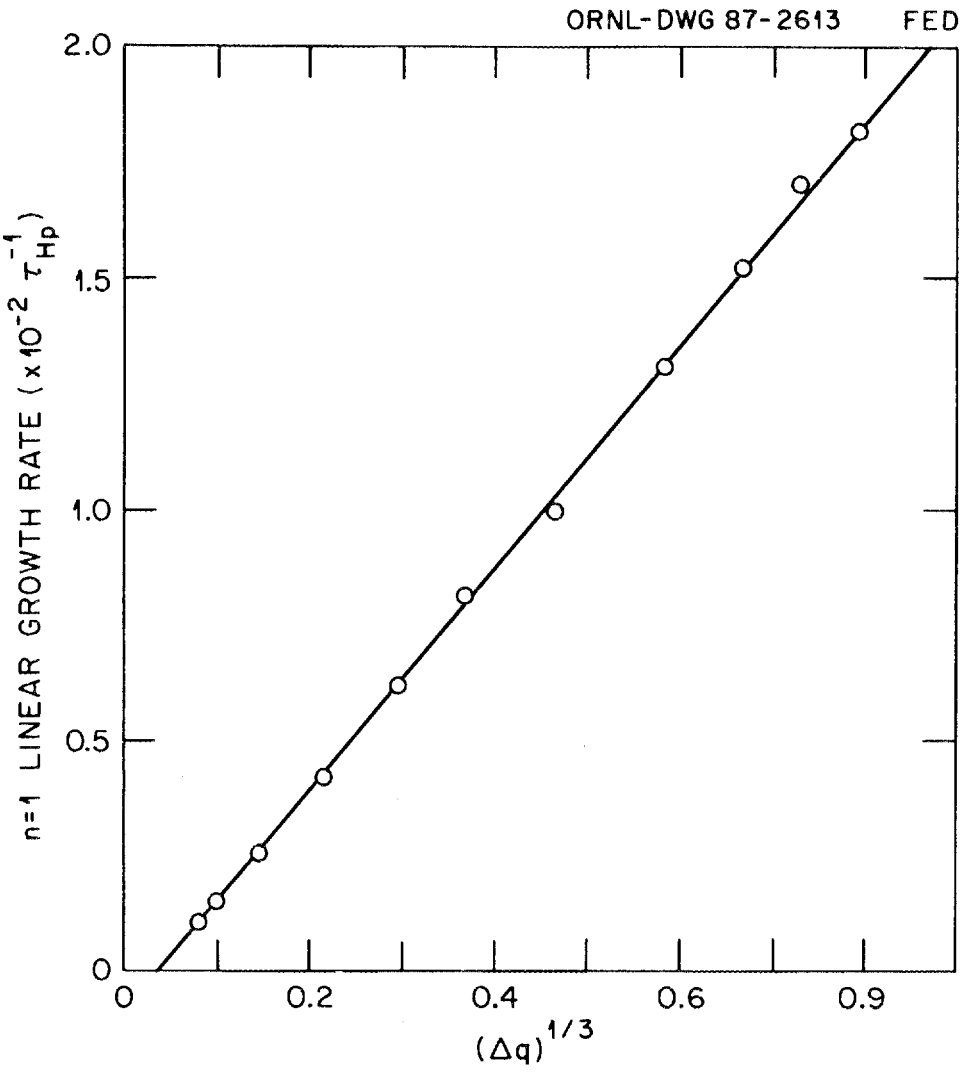


Fig. 2. $n = 1$ linear growth rate vs $(\Delta q)^{1/3}$ for hollow $q$ profile equilibria with $q_{\min} = 1$ and $\rho_{\min} = 0.5$. Here $\beta = 0$, $\epsilon = 0.4$, $\kappa = 1.0$, and $\delta = 0$.

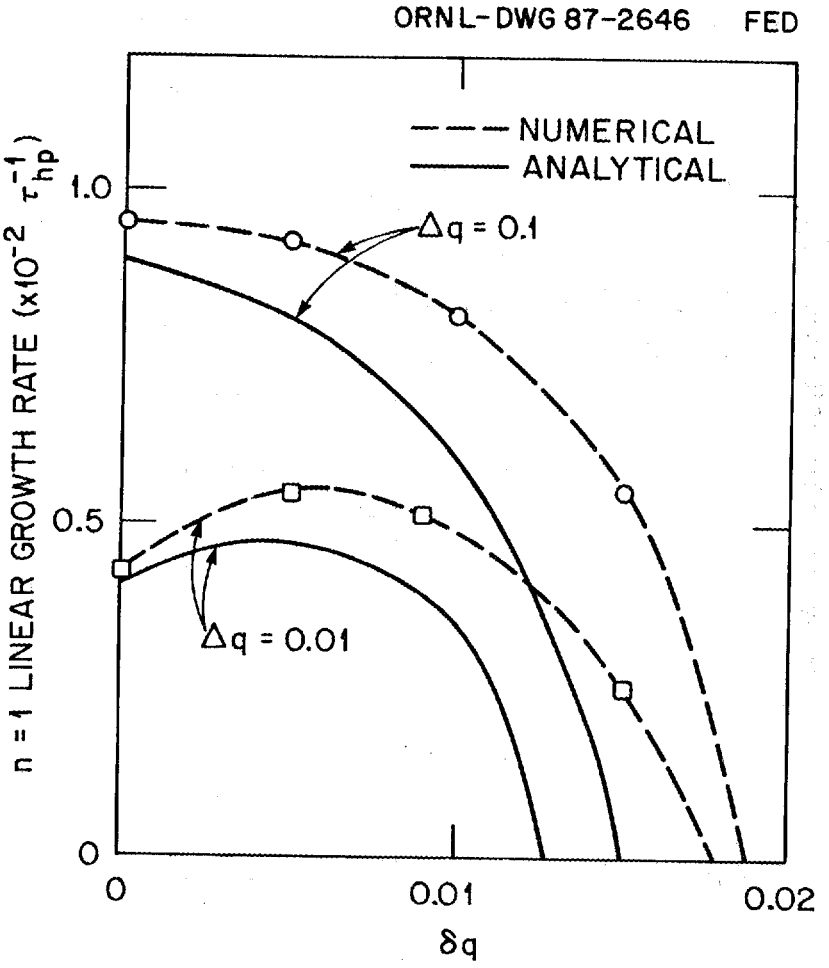


Fig. 3. Analytic and numerical linear growth rates vs $\delta q = q_{\min} - 1$ for hollow $q$ profile equilibria with $\Delta q = 0.1$ and 0.01. Other parameters are $\rho_{\min} = 0.5$, $\beta = 0$, $\epsilon = 0.4$, $\kappa = 1.0$, and $\delta = 0$.

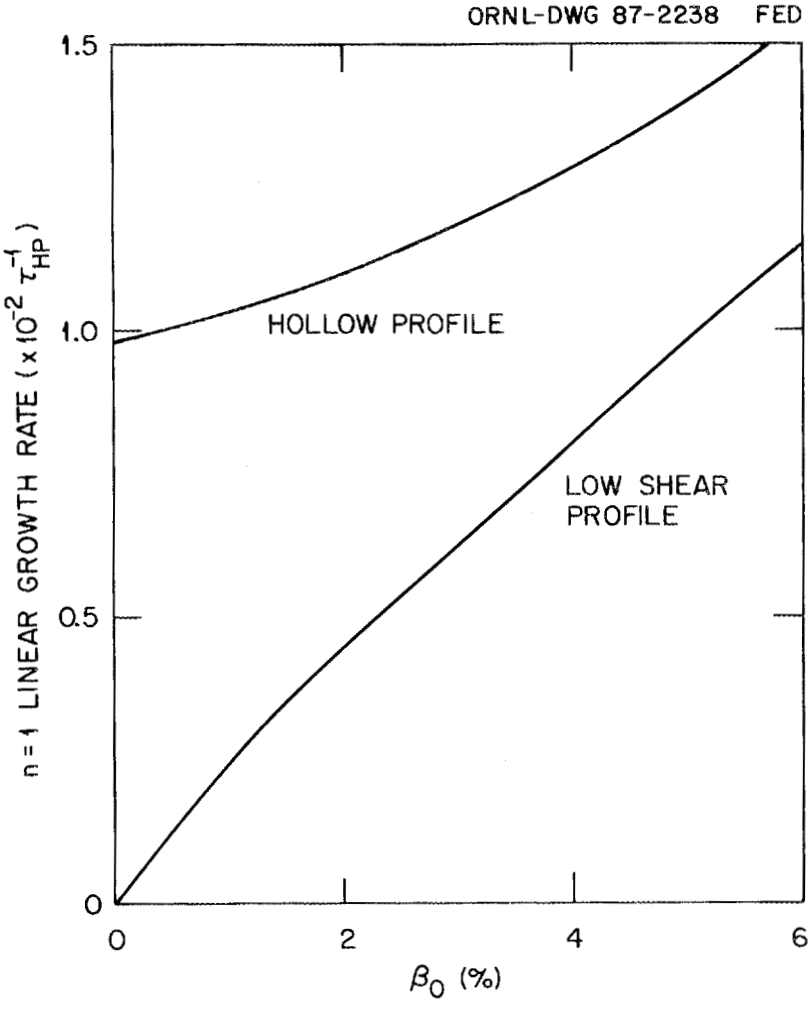


Fig. 4. $n = 1$ linear growth rates vs $\beta_0$ for hollow and low-shear $q$ profiles with $\epsilon = 0.4$, $\kappa = 1.0$, and $\delta = 0$.

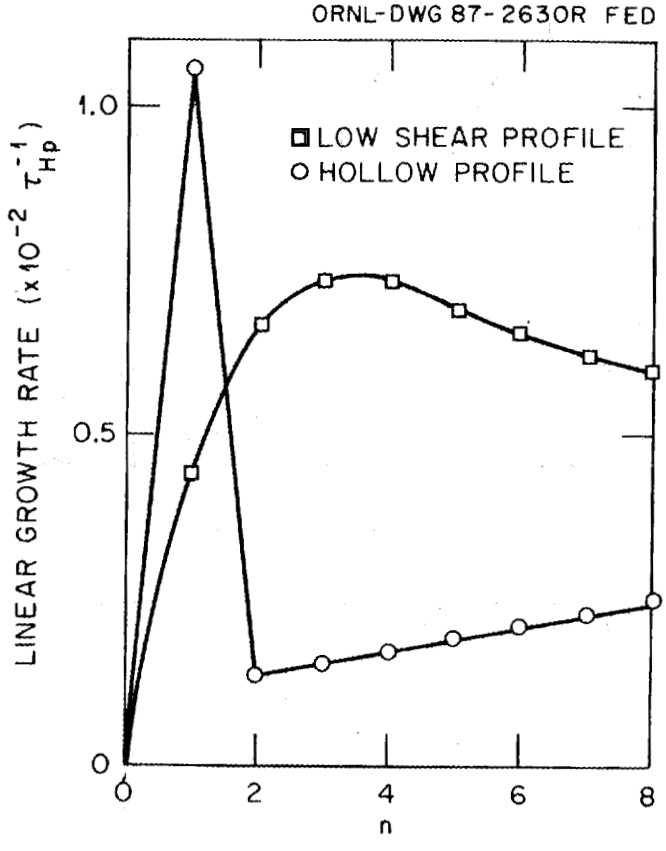


Fig. 5. Comparison of linear growth rates vs $n$ for hollow and low-shear safety factor profiles at $\beta_0 = 2\%$.

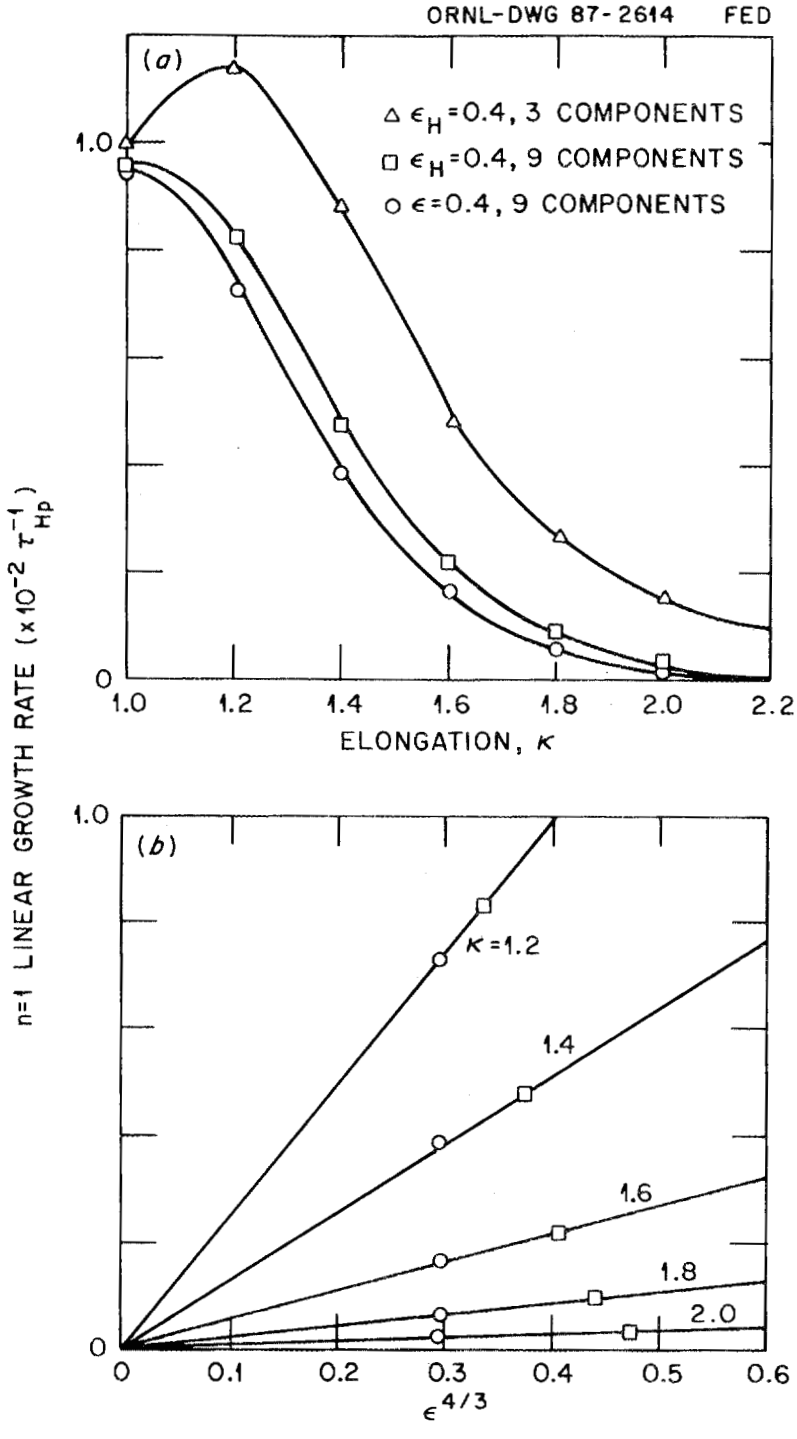


Fig. 6. $n = 1$ linear growth rates vs (a) elongation $\kappa$ for hollow $q$ profile equilibria at $\beta = 0$, $q_{\min} = 1.0$, $\Delta q = 0.1$, and $\rho_{\min} = 0.5$; and (b) $\epsilon^{4/3}$ for several elongations taken from Fig. 6a.

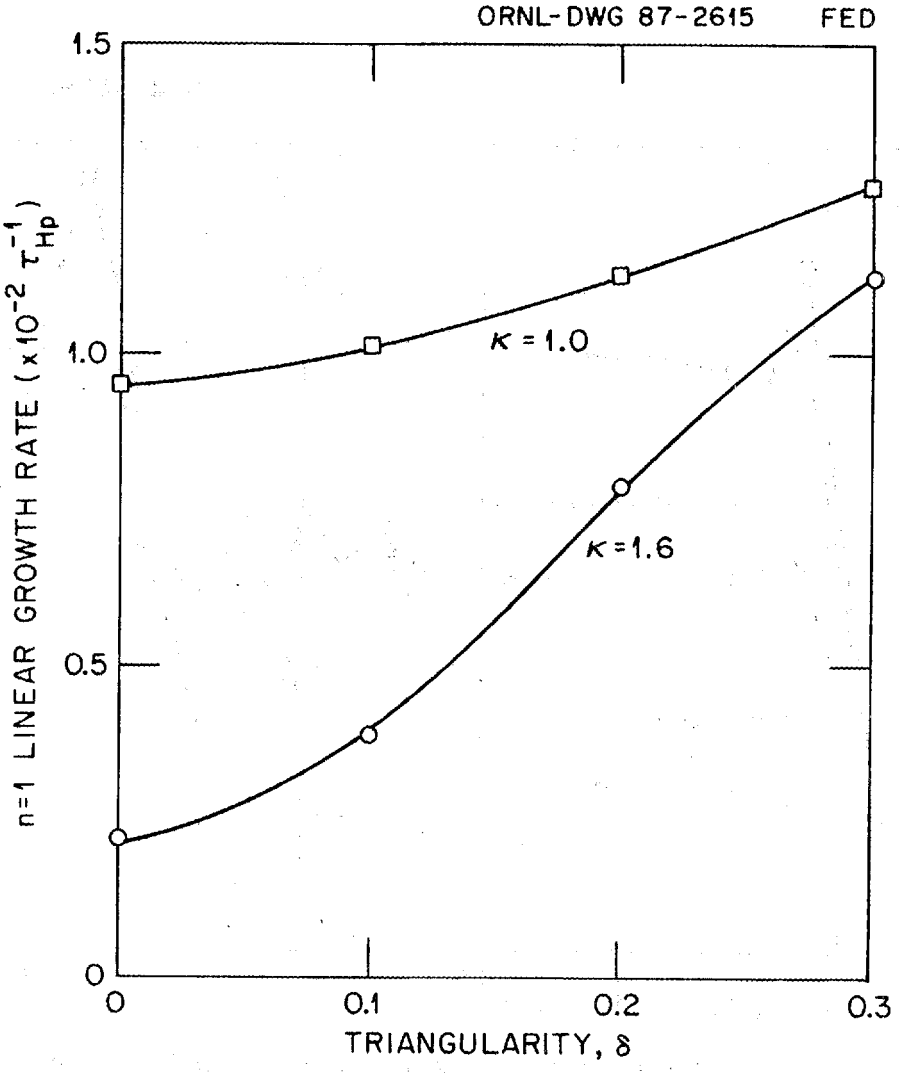


Fig. 7. $n = 1$ linear growth rates vs triangularity $\delta$ for hollow $q$ profile equilibria with elongation $\kappa = 1.0$ and $\kappa = 1.6$. Here $\epsilon_H = 0.4$, $\beta = 0$, $q_{\min} = 1.0$, $\Delta q = 0.1$, and $\rho_{\min} = 0.5$.

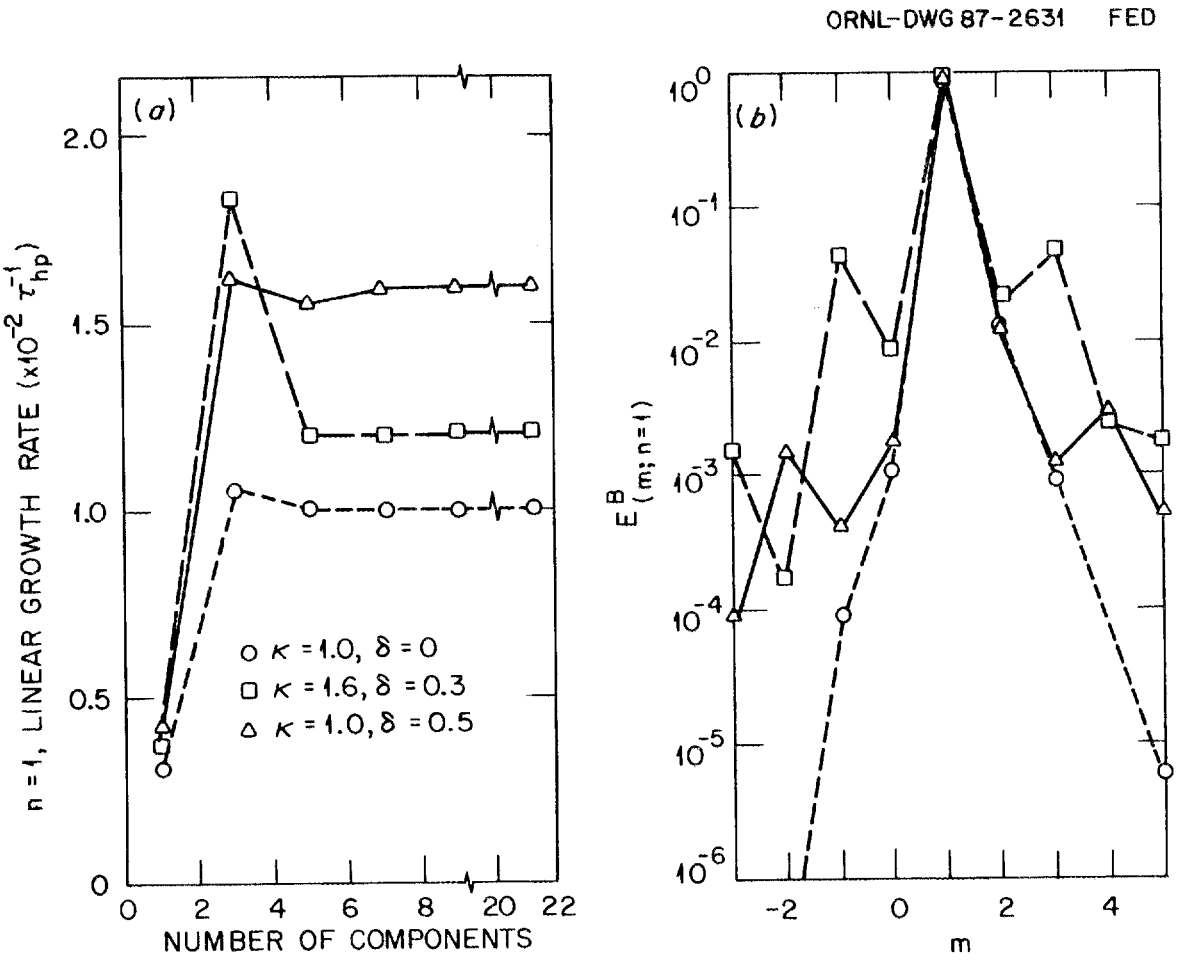


Fig. 8. (a) $n = 1$ linear growth rates vs number of poloidal components for hollow $q$ profile equilibria of different shapes. In all cases, $\epsilon_H = 0.4$, $\beta = 0$, $q_{\min} = 1.0$, $\Delta q = 0.1$, and $\rho_{\min} = 0.5$; (b) magnetic norm $E^B_{(m;n=1)}$ vs $m$ for cases shown in Fig. 8a.

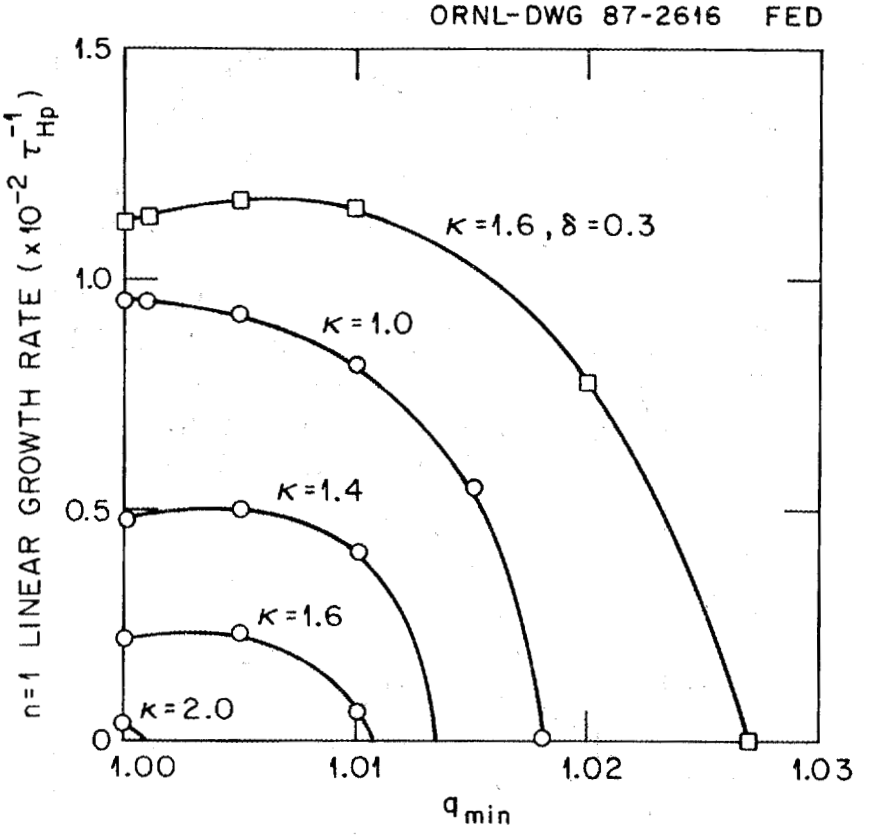


Fig. 9. $n = 1$ linear growth rates vs $q_{\min}$ for hollow $q$ profile equilibria of several shapes. In all cases, $\epsilon_H = 0.4$, $\beta = 0$, $\Delta q = 0.1$, and $\rho_{\min} = 0.5$.

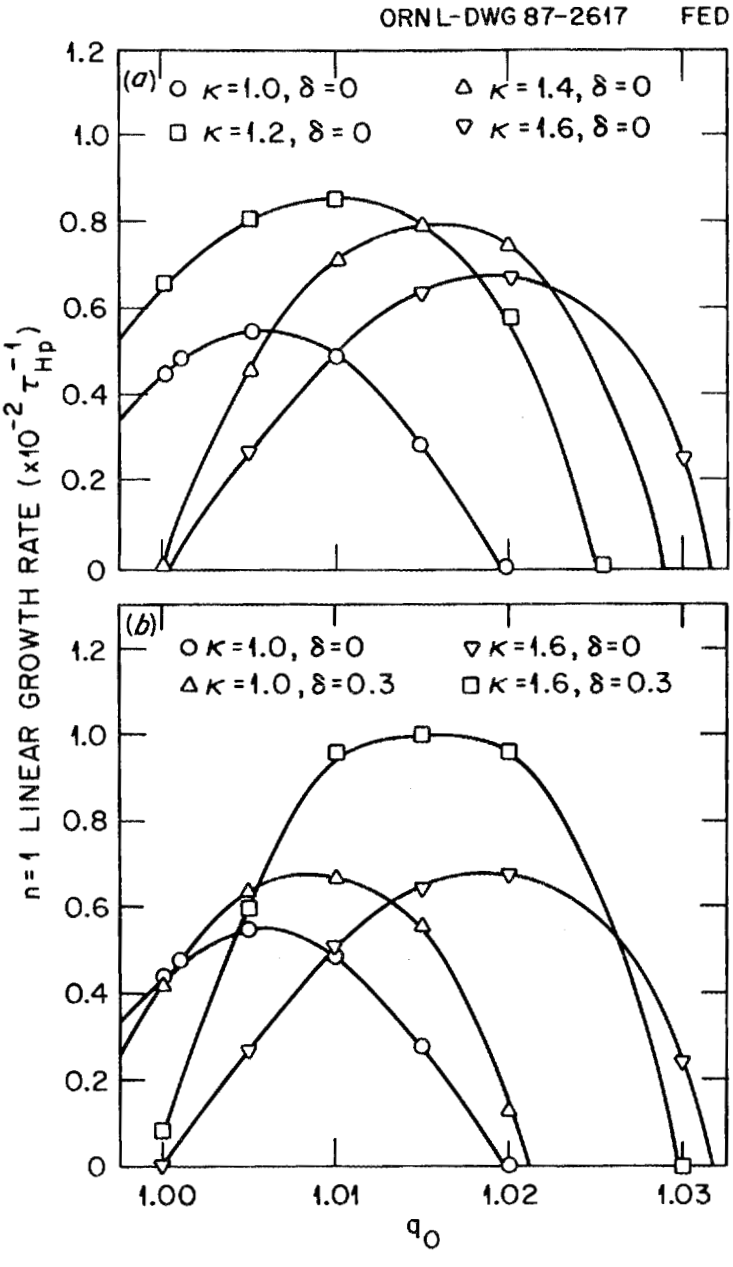


Fig. 10. (a) $n = 1$ linear growth rates vs $q_0$ for low-shear $q$ profiles having $\rho_0 = 0.75$, $\lambda = 6$, and $\Delta q_\ell = 0$ and several elongations $\kappa$. Here $\beta_0 = 2\%$ and $\epsilon_H = 0.4$; (b) same comparison as Fig. 10a, but including equilibria with nonzero triangularity $\delta = 0.3$.

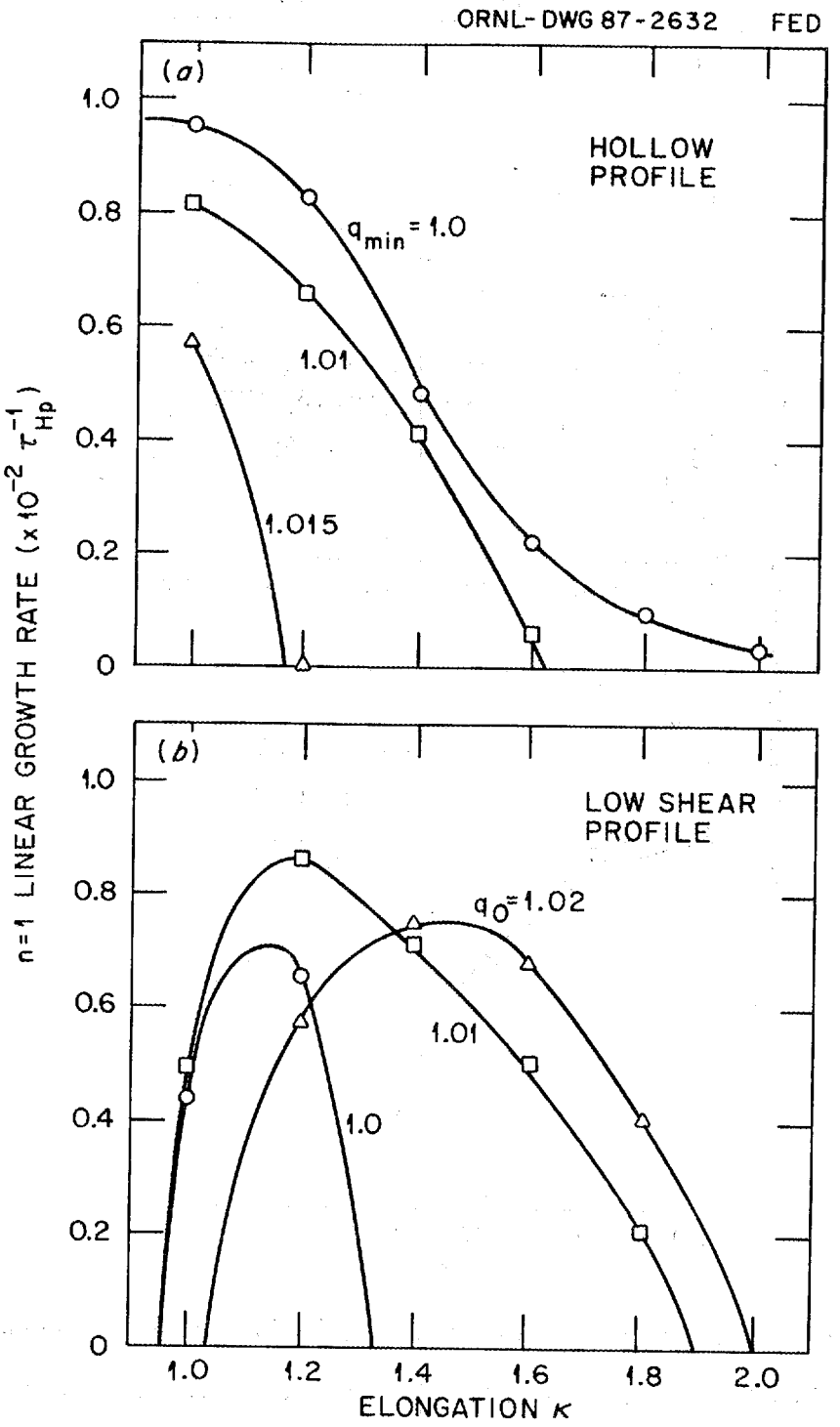


Fig. 11. $n = 1$ linear growth rates vs elongation $\kappa$ for (a) hollow $q$ profiles with several $q_{\min}$ and $\beta = 0$, $\epsilon_H = 0.4$, $\Delta q = 0.1$, and $\rho_{\min} = 0.5$; and (b) low-shear $q$ profiles with several $q_0$ and $\beta = 2\%$, $\epsilon_H = 0.4$, $\rho_0 = 0.75$, $\lambda = 6$, and $\Delta q_\ell = 0$.

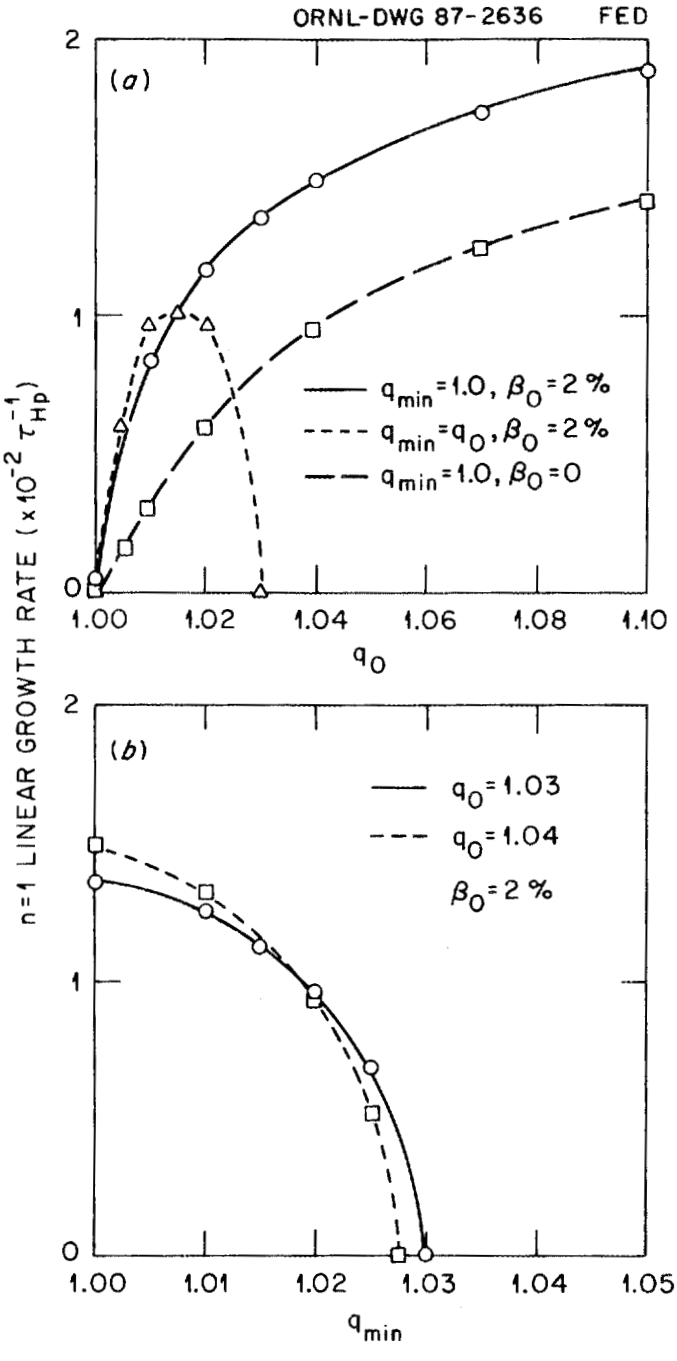


Fig. 12. $n = 1$ linear growth rates vs (a) $q_0$ for low shear and locally hollow $q$ profile equilibria having $\beta_0 = 0$ and $\beta_0 = 2\%$ and $\Delta q_\ell = q_0 - 1$, $\rho_0 = 0.75$, $\lambda = 6$, $\kappa = 1.6$, and $\delta = 0.3$; and (b) $q_{\min} = q_0 - \Delta q_\ell$ for $q_0 = 1.03$ and 1.04 and other parameters as in Fig. 12a.

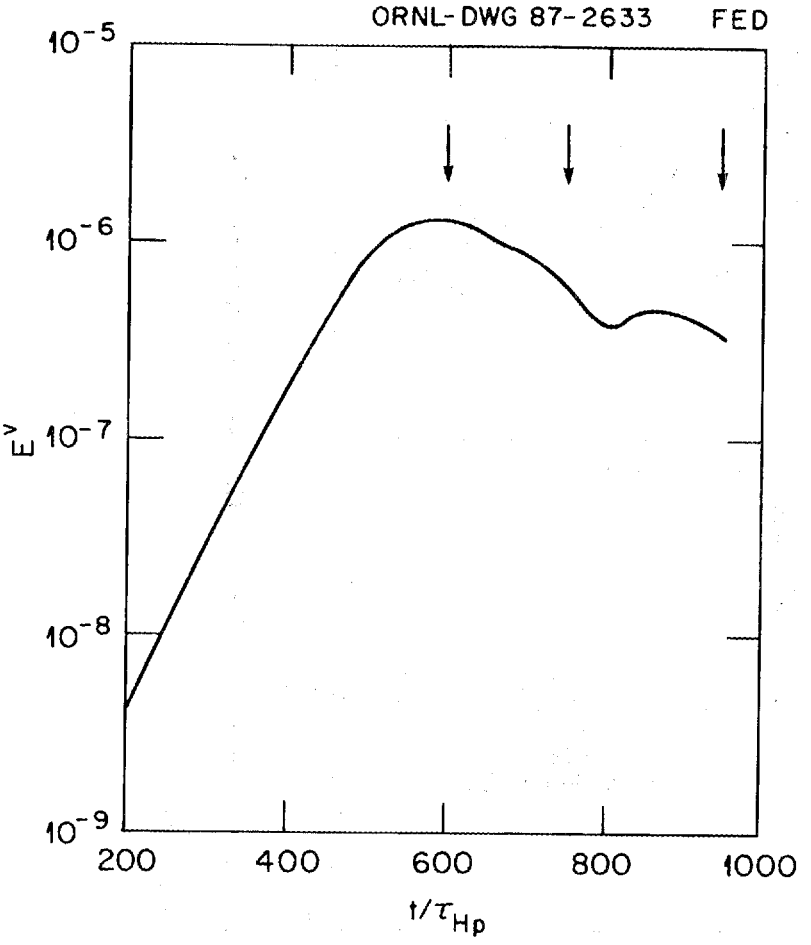


Fig. 13. Velocity norm $E^v$ vs time for nonlinear calculation of internal kink evolution for the low-shear $q$ profile case having $\beta_0 = 2\%$, $\epsilon_H = 0.4$, $q_0 = 1.015$, $\rho_0 = 0.75$, $\lambda = 6$, $\Delta q_\ell = 0$, $\kappa = 1.6$, and $\delta = 0.3$. Arrows denote times for velocity vector and flux surface plots in Figs. 14 and 15.

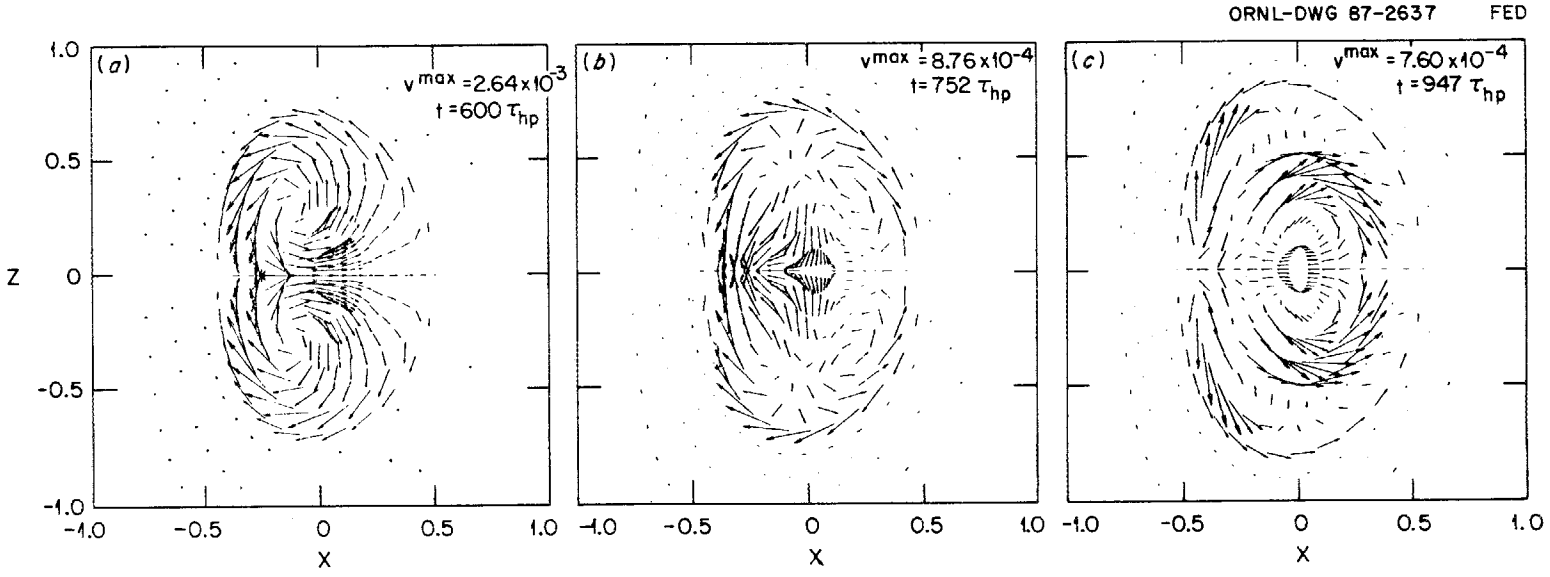


Fig. 14. Velocity vector plots in the $\zeta = 0$ plane for the case shown in Fig. 13.

Times are $600\tau_{H_p}$, $752\tau_{H_p}$, and $947\tau_{H_p}$.

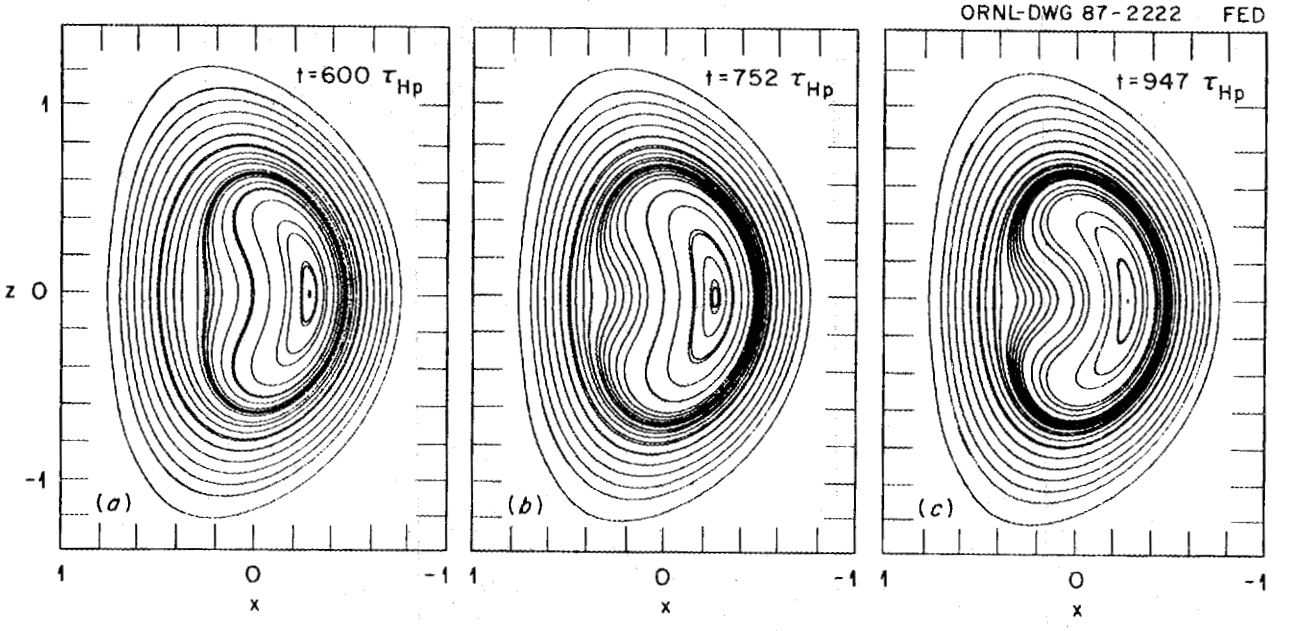


Fig. 15. Magnetic field line plots in the $\zeta = 0$ plane for the case shown in Fig. 13. Times are $600\tau_{H_p}$, $752\tau_{H_p}$, and $947\tau_{H_p}$.

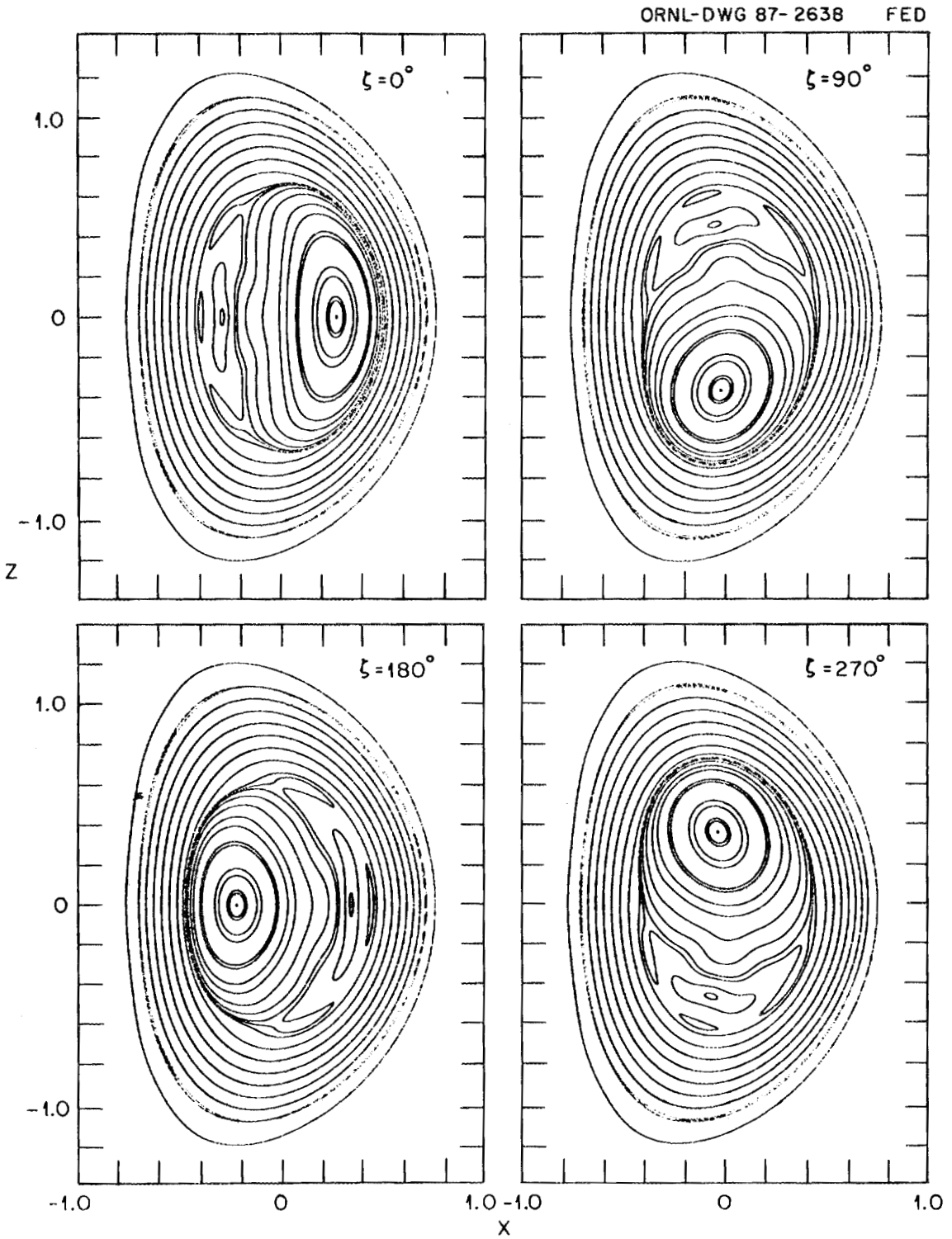


Fig. 16. Magnetic field line plots in the $\zeta = 0°$, 90°, 180°, and 270° planes showing the helical nature of the internal kink displacement. The case shown has $\beta = 0$, $\epsilon_H = 0.4$, $\kappa = 1.6$, $\delta = 0.3$, and a hollow $q$ profile with $q_{\min} = 1.0$, $\Delta q = 0.1$, and $\rho_{\min} = 0.5$. For these cases, the magnetic bubble appears when $q_{\min} = 1$.

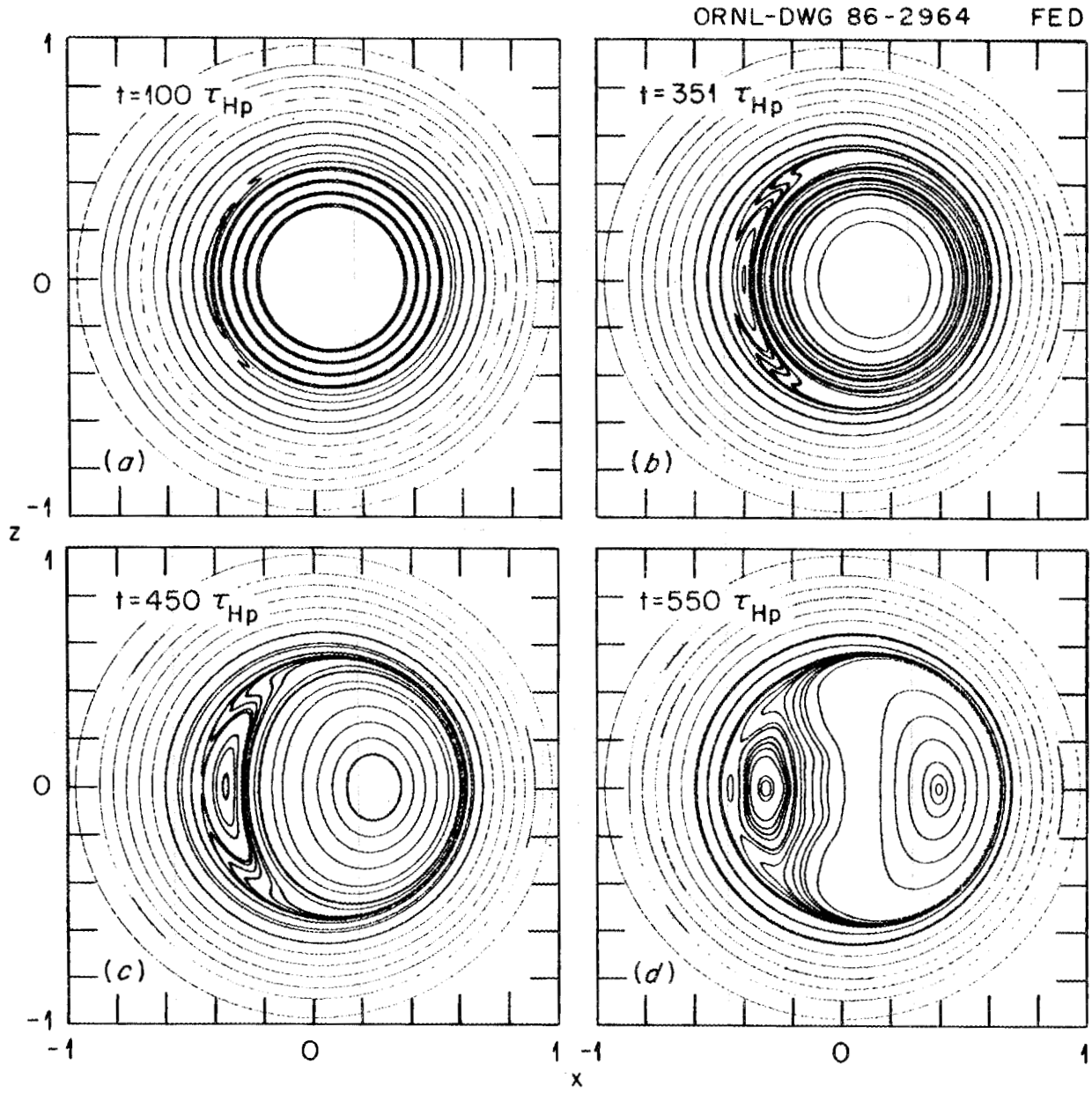


Fig. 17. Magnetic field line plots of internal kink evolution at four times for the hollow $q$ profile case. Except for circular cross section $\kappa = 1$, $\delta = 0$, the parameters are the same as in Fig. 16.

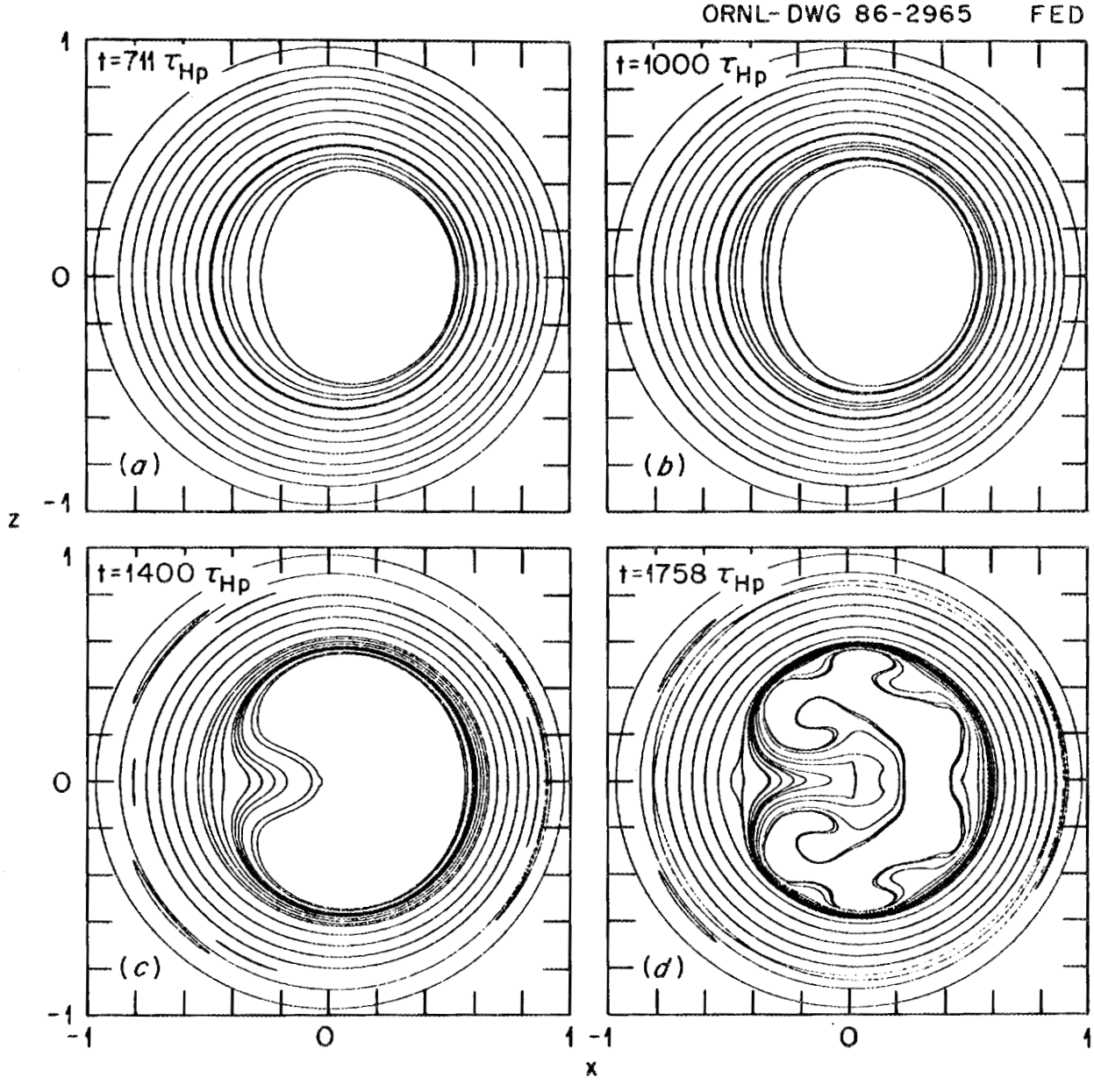


Fig. 18. Magnetic field line plots of internal kink evolution at four times for the low-shear $q$ profile case. Here $\beta_0 = 2\%$, $\epsilon = 0.4$, $\kappa = 1$, $\delta = 0$, $q_0 = 1.0$, $\rho_0 = 0.75$, $\lambda = 6$, and $\Delta q_\ell = 0$.

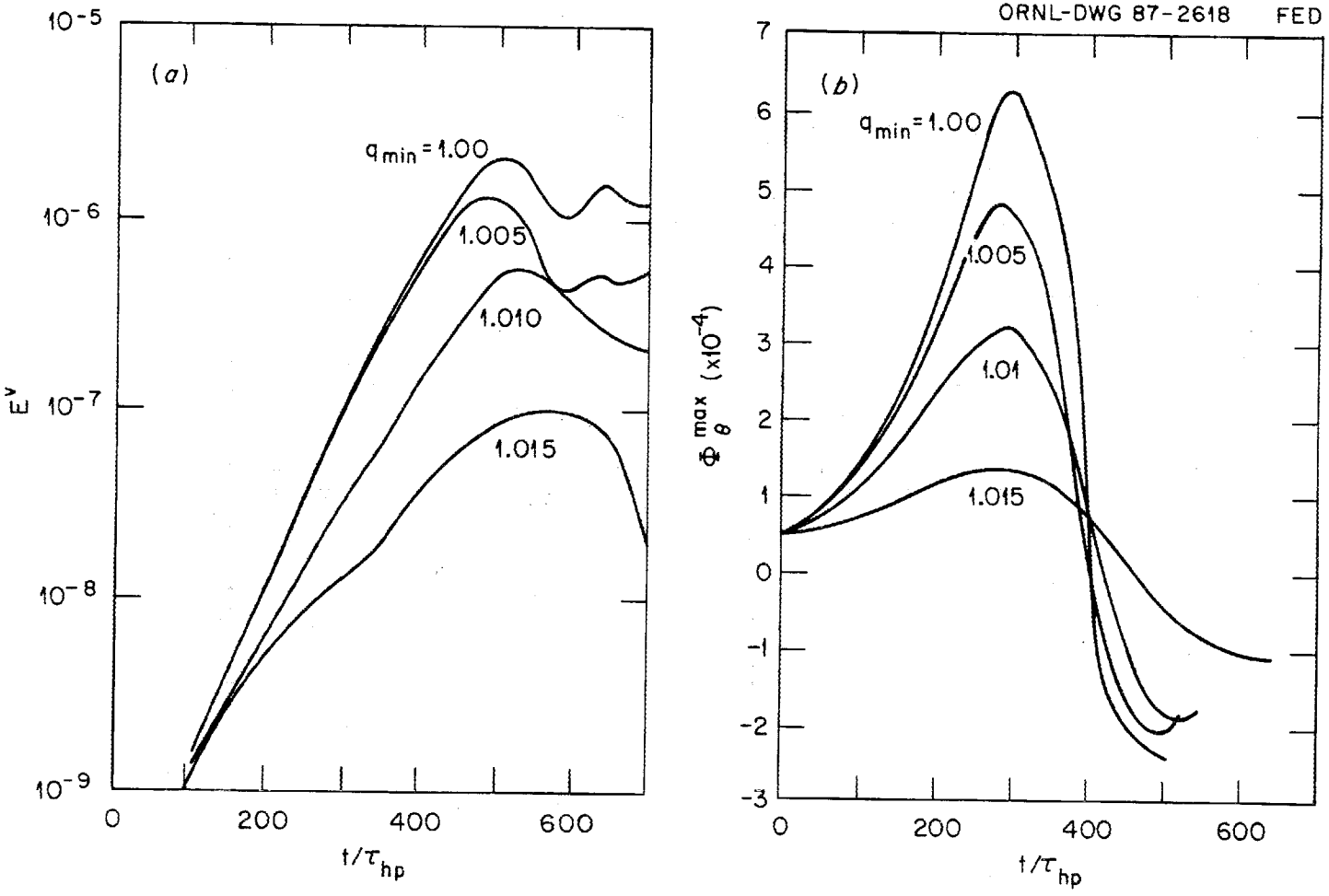


Fig. 19. (a) Velocity norms $E^v$ vs time for four hollow $q$ profile cases. The parameters match those of Fig. 17 except for $q_{\min}$, which is indicated; (b) $\Phi_\theta^{max}$, the peak value of the (1;1) component of $\Phi_\theta$, vs time for the cases shown in Fig. 19a. The time scales have been shifted to give equal initial values.

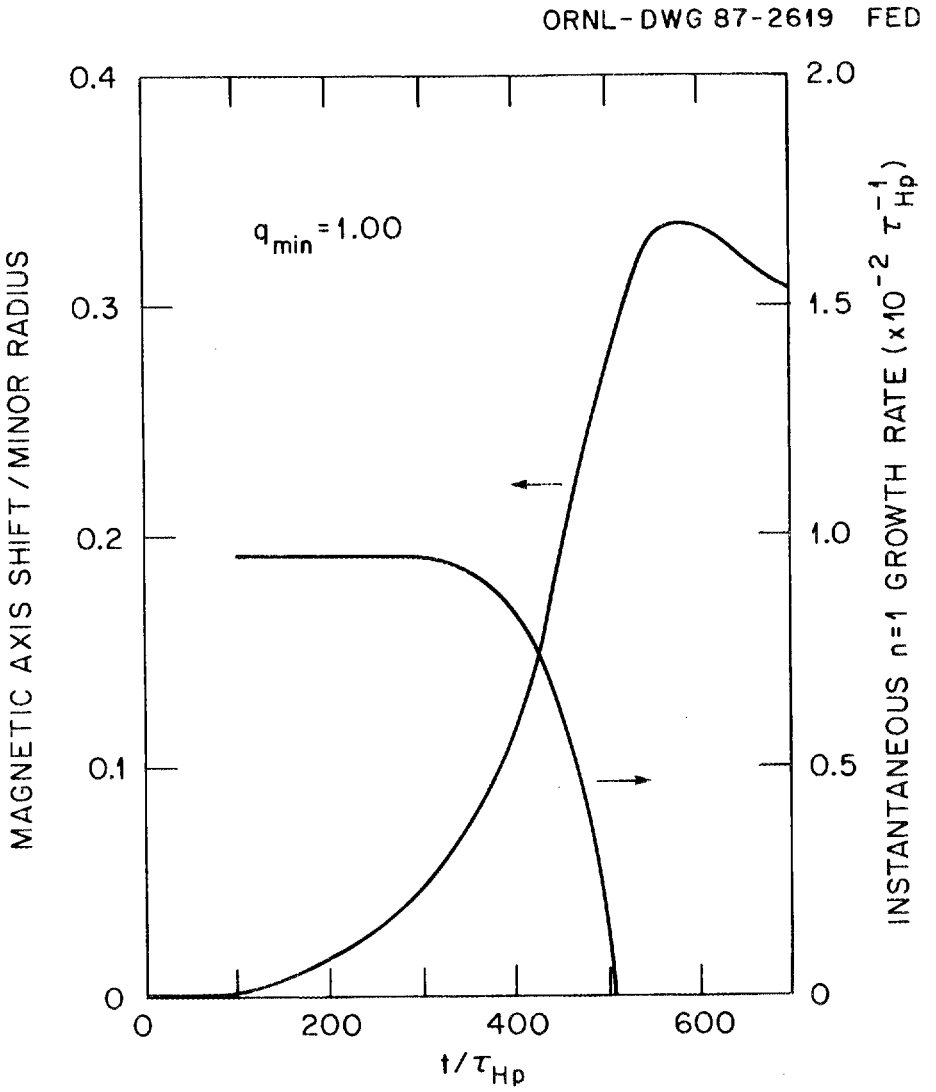


Fig. 20. Instanteous $n = 1$ growth rate and magnetic axis shift vs time for the $q_{\min} = 1.0$ case shown in Fig. 19.

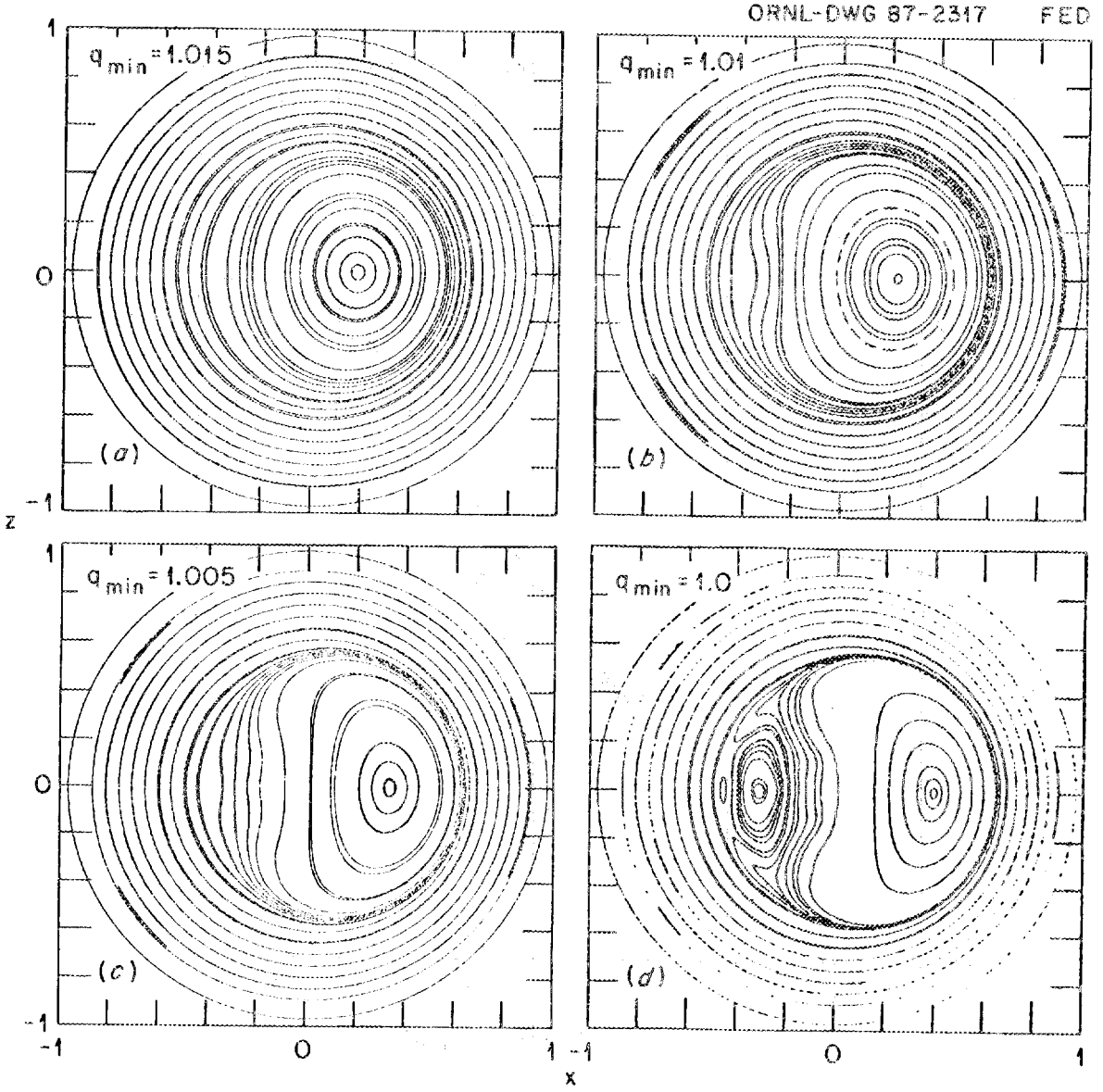


Fig. 21. Magnetic field line plots in the $\zeta = 0$ plane at saturation for the four cases shown in Fig. 19.

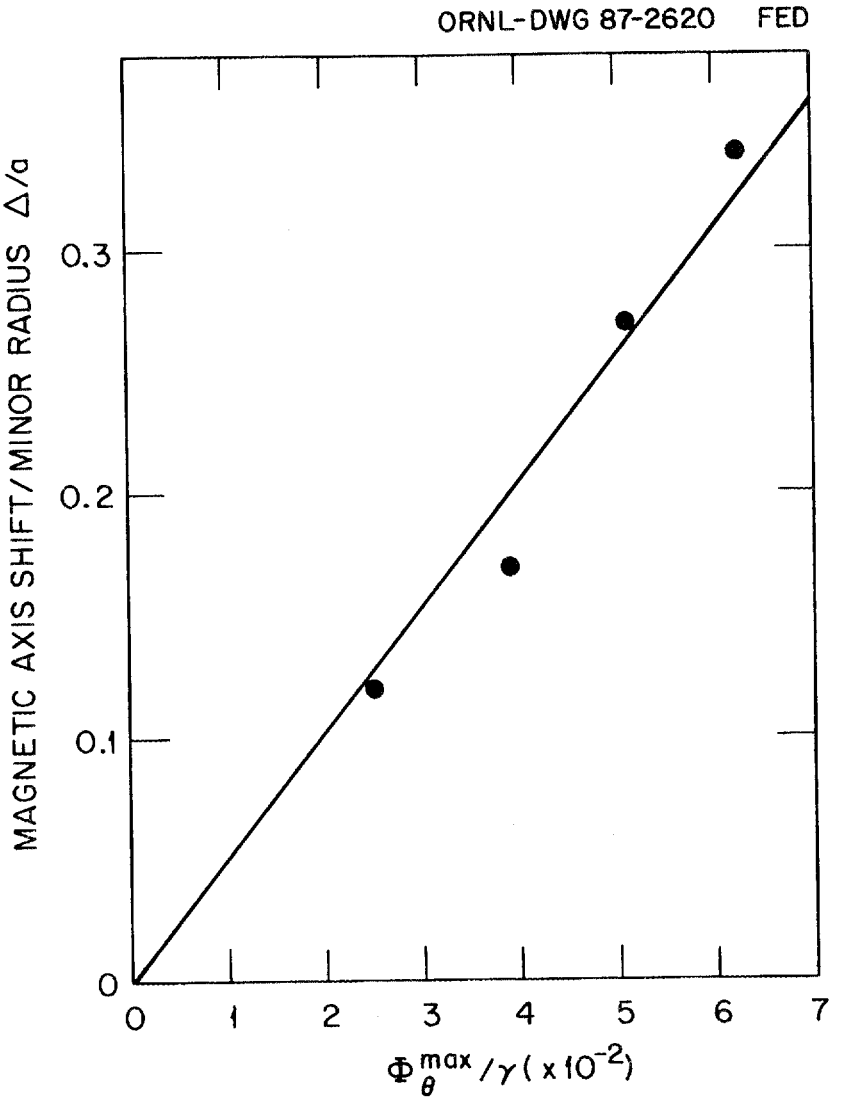


Fig. 22. Magnetic axis shift at saturation vs total plasma displacement as estimated by giving the peak value of $\Phi_\theta^{max}$ divided by the $n = 1$ linear growth rate. The four cases are from Fig. 19.

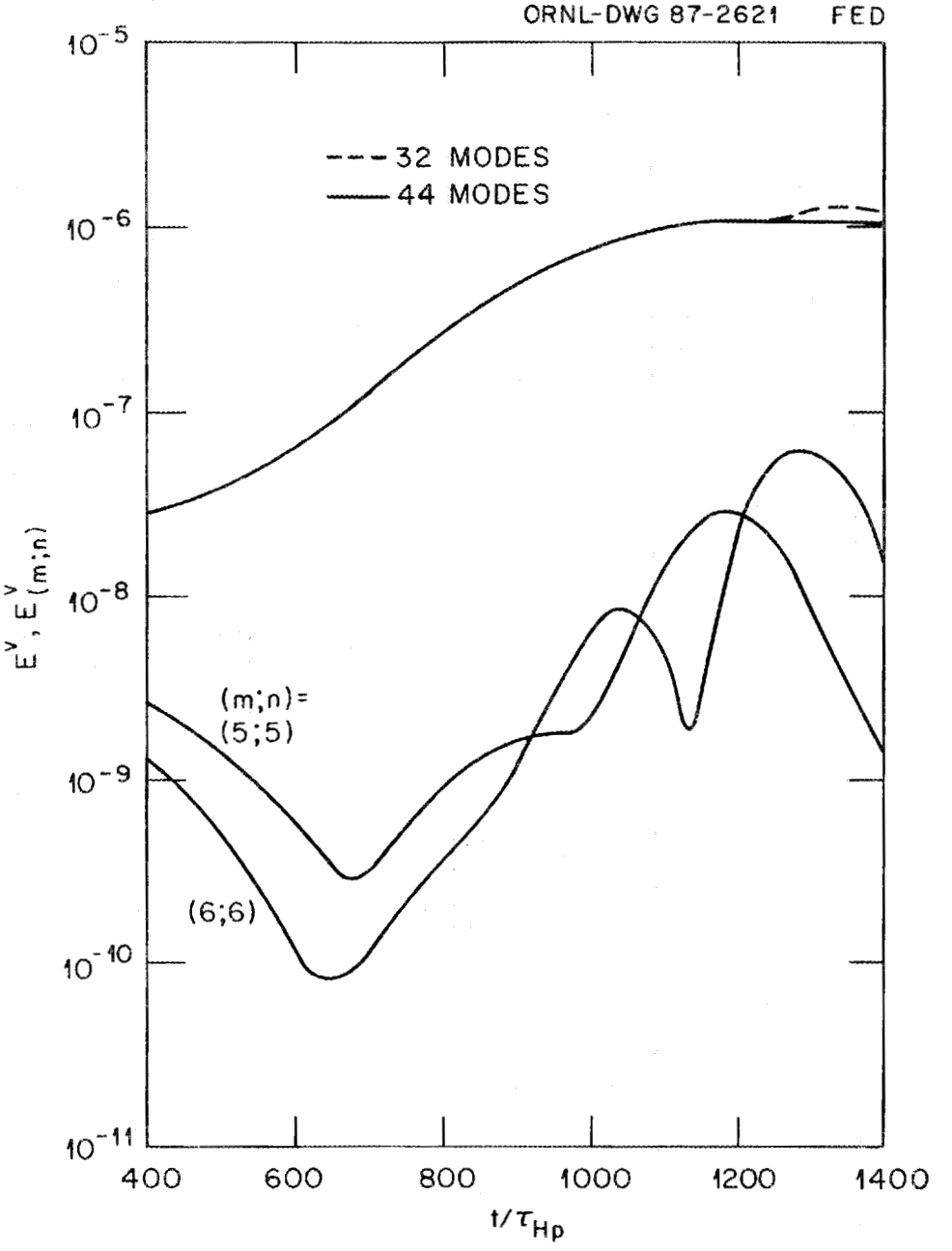


Fig. 23. Velocity norms $E^v$ from the 32- and 44-mode cases and $E^v_{(m;n)}$ from 44-mode case vs time for the low-shear $q$ profile case shown in Fig. 18.

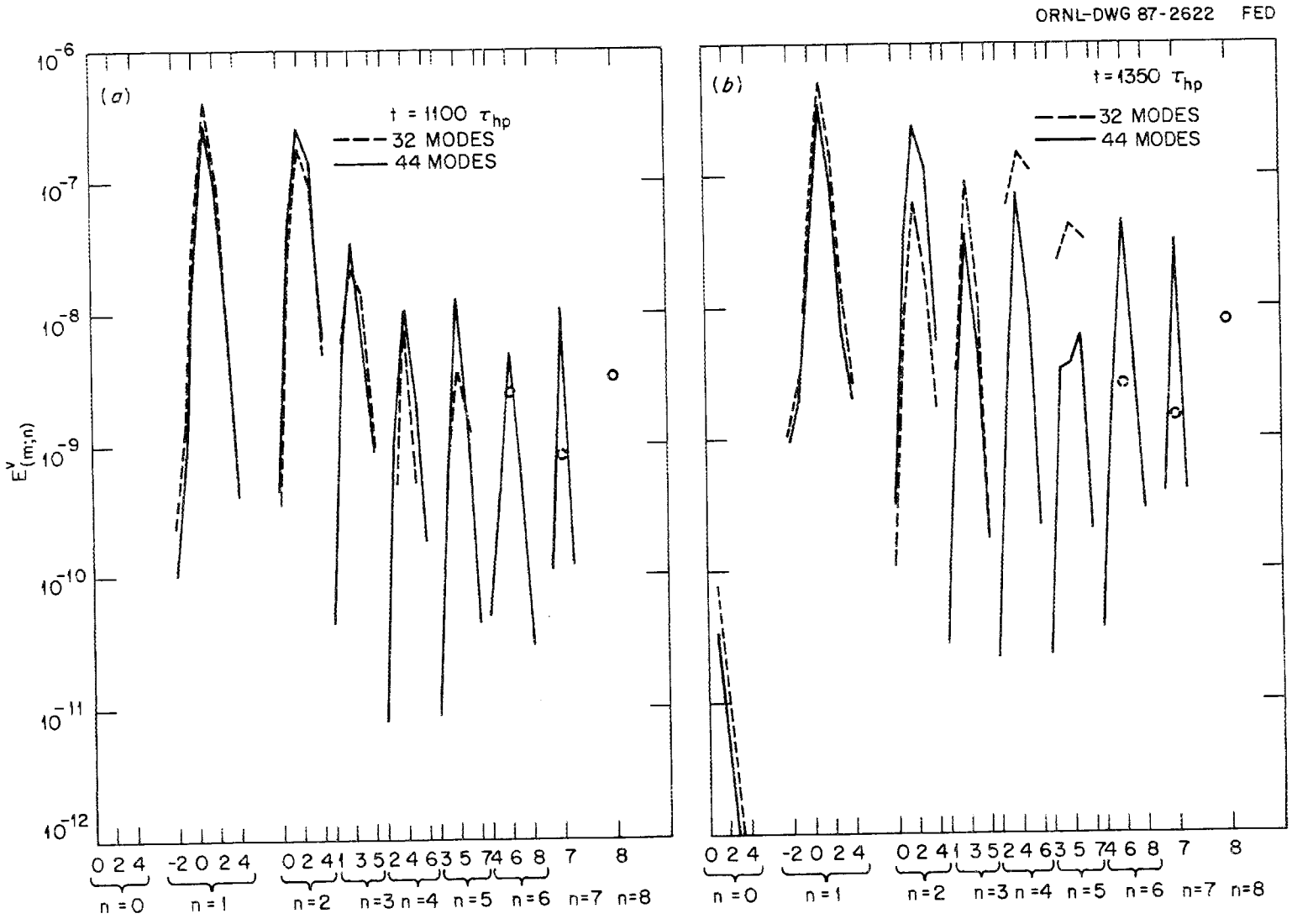


Fig. 24. Velocity norms $E^{v}_{(m;n)}$ vs $m$ and $n$ at two times for the 32- and 44-mode cases shown in Fig. 23. Circles denote single poloidal component $m$; (a) $t = 1100\tau_{H_p}$; and (b) $t = 1350\tau_{H_p}$.

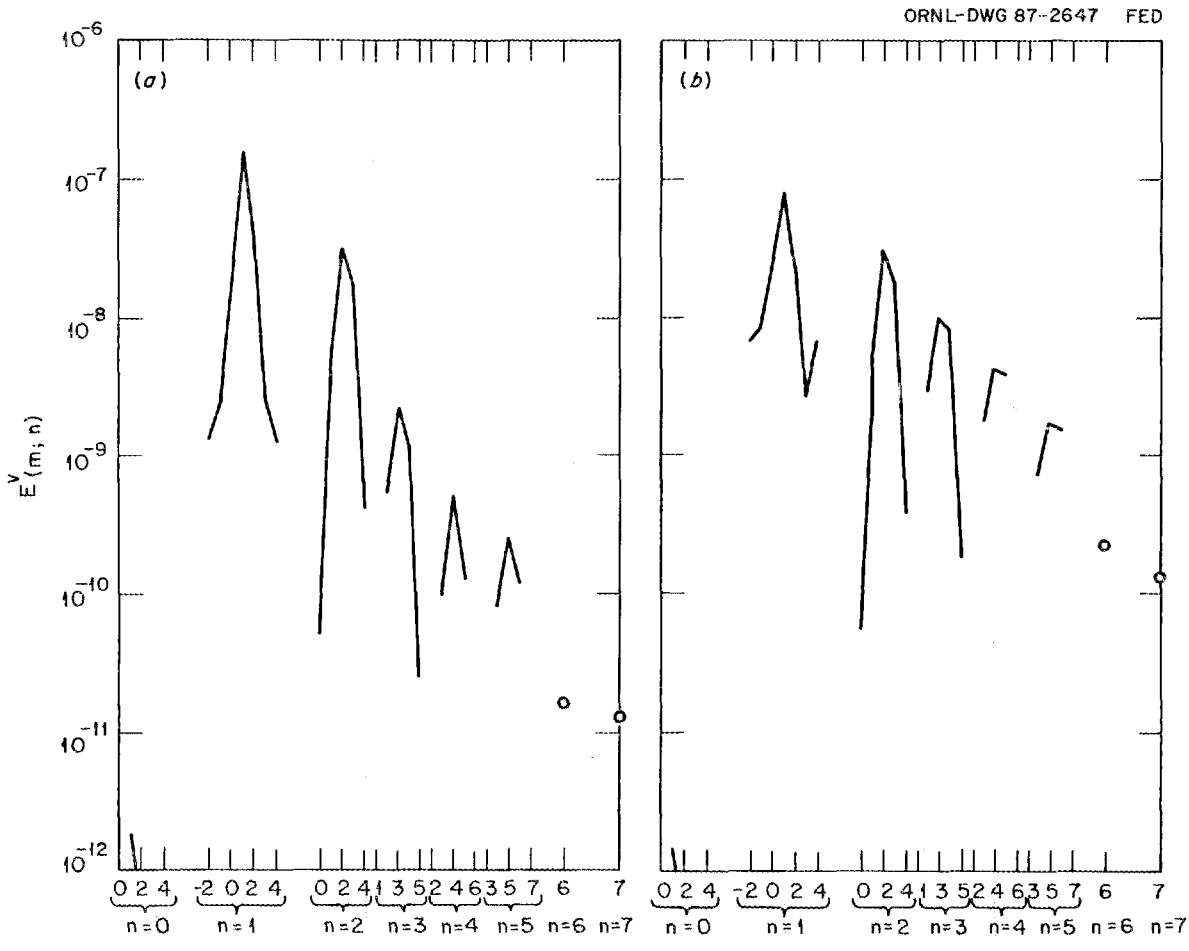


Fig. 25. Velocity norms $E^{v}_{(m;n)}$ vs $m$ and $n$ at two times for the low-shear hollow profile case given by $\beta = 0$, $\epsilon = 0.4$, $\kappa = 1$, $\delta = 0$, and Eq. (23) with $q_{\min} = 1.005$, $\Delta q_{\text{in}} = 0.003$, $\Delta q_{\text{out}} = 0.1$, and $\rho_{\min} = 0.5$; (a) $t = 1300\tau_{H_p}$; and (b) $t = 1600\tau_{H_p}$.

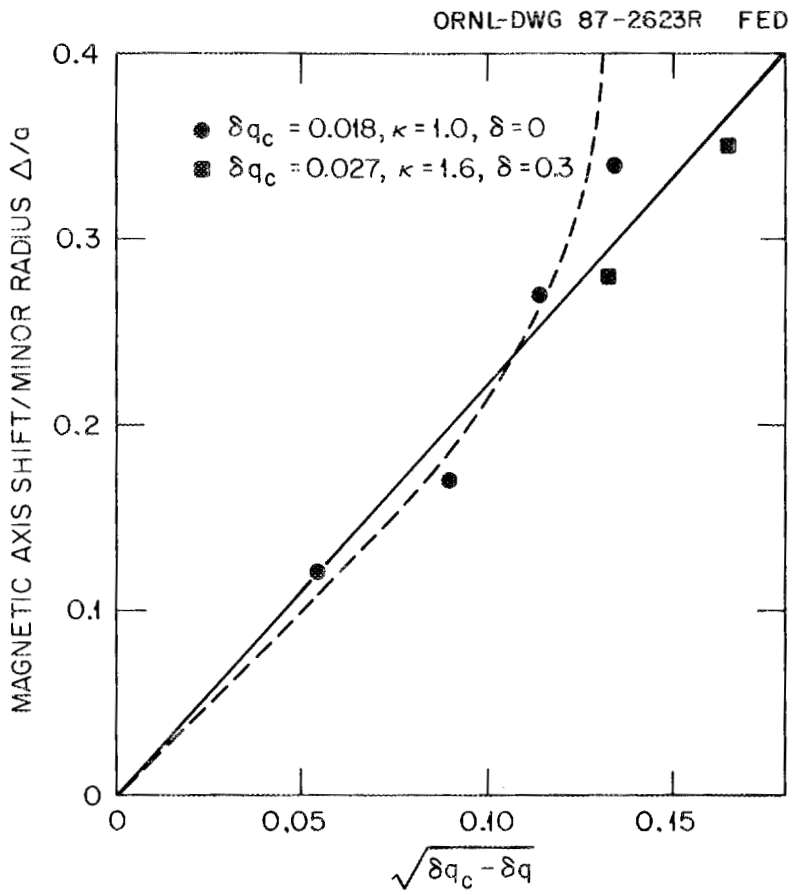


Fig. 26. Magnetic axis shifts at saturation vs $\sqrt{\delta q_c - \delta q}$ for hollow profile cases including four cases with circular cross section and two cases with $\kappa = 1.6$, $\delta = 0.3$. Other parameters are $\beta = 0$, $\epsilon_H = 0.4$, $\Delta q = 0.1$, and $\rho_{\min} = 0.5$. The solid and dashed curves plot the analytic expressions given by Eqs. (20) and (22), respectively.

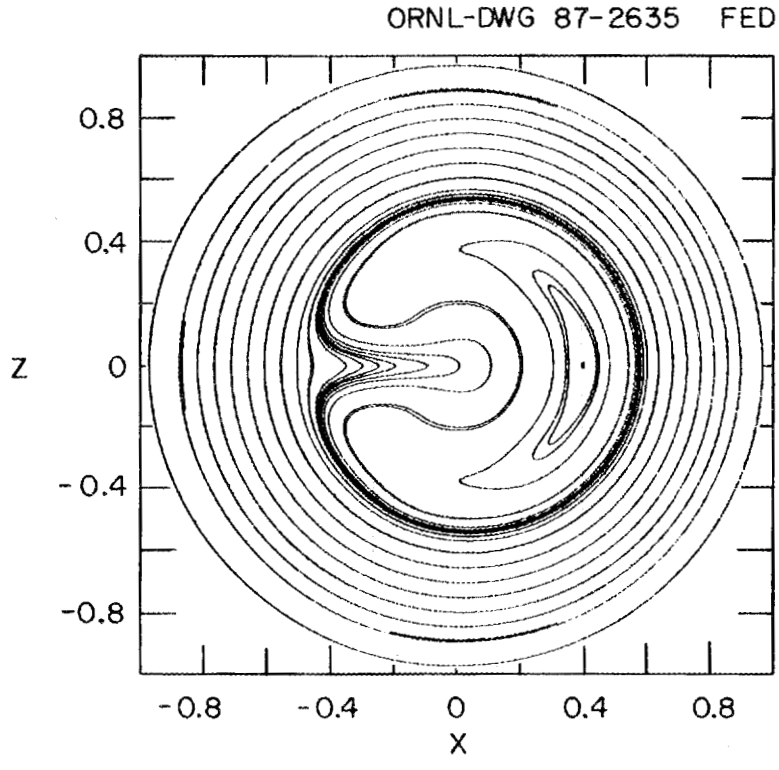


Fig. 27. Magnetic field line plot at saturation for the low-shear hollow profile case shown in Fig. 25.

ORNL/TM-10585
Dist. Category UC-20g

## INTERNAL DISTRIBUTION

1–5. B. A. Carreras
6–10. L. A. Charlton
11. R. A. Dory
12. R. H. Fowler
13. S. P. Hirshman
14–18. J. A. Holmes
19. V. E. Lynch
20. D. A. Spong
21. W. I. van Rij
22. G. E. Whitesides
23. J. Sheffield
24–25. Laboratory Records Department
26. Laboratory Records, ORNL-RC
27. Central Research Library
28. Document Reference Section
29. Fusion Energy Division Library
30–31. Fusion Energy Division Publications Office
32. ORNL Patent Office

## EXTERNAL DISTRIBUTION

33. R. J. Hastie, Culham Laboratory, Abingdon, Oxon OX14 3DB, England
34. T. C. Hender, Culham Laboratory, Abingdon, Oxon OX14 3DB, England
35. P. H. Diamond, Institute for Fusion Studies, University of Texas, Austin, TX 78712
36. Office of the Assistant Manager for Energy Research and Development, U.S. Department of Energy, Oak Ridge Operations, P.O. Box E, Oak Ridge, TN 37831
37. J. D. Callen, Department of Nuclear Engineering, University of Wisconsin, Madison, WI 53706
38. R. W. Conn, Department of Chemical, Nuclear, and Thermal Engineering, Boelter Hall, University of California, Los Angeles, CA 90024
39. S. O. Dean, Director, Fusion Power Associates, Inc., 2 Professional Drive, Suite 249, Gaithersburg, MD 20760
40. H. K. Forsen, Bechtel Group, Inc., Research & Engineering, P.O. Box 3965, San Francisco, CA 94119
41. J. R. Gilleland, Lawrence Livermore National Laboratory, P.O. Box 5511, Livermore, CA 94550
42. R. W. Gould, Department of Applied Physics, California Institute of Technology, Pasadena, CA 91125
43. R. A. Gross, Plasma Research Laboratory, Columbia University, New York, NY 10027

44. D. M. Meade, Princeton Plasma Physics Laboratory, P.O. Box 451, Princeton, NJ 08544
45. W. M. Stacey, Jr., Georgia Institute of Technology, School of Nuclear Engineering and Health Physics, Atlanta, GA 30332
46. D. Steiner, Rensselaer Polytechnic Institute, Nuclear Engineering Department, NES Building, Tibbets Avenue, Troy, NY 12181
47. R. Varma, Physical Research Laboratory, Navrangpura, Ahmedabad 380009, India
48. Bibliothek, Max-Planck Institut für Plasmaphysik, D-8046 Garching, Federal Republic of Germany
49. Bibliothek, Institut für Plasmaphysik, KFA, Postfach 1913, D-5170 Julich, Federal Republic of Germany
50. Bibliothek, KfK Karlsruhe GmbH, Postfach 3640, D-7550 Karlsruhe 1, Federal Republic of Germany
51. Bibliotheque, Centre de Récherches en Physique des Plasmas, Ecole Polytechnique Federale de Lausanne, 21 Avenue des Bains, CH-1007 Lausanne, Switzerland
52. F. Prevot, CEN/Cadarache, Departement de Recherches sur la Fusion Contrôlée, F-13108 Saint-Paul-lez-Durance Cedex, France
53. Bibliothèque, CEN/Cadarache, F-13108 Saint-Paul-lez-Durance Cedex, France
54. Library, Culham Laboratory, UKAEA, Abingdon, Oxfordshire, OX14 3DB, England
55. Library, JET Joint Undertaking, Abingdon, Oxfordshire OX14 3EA, England
56. Library, FOM-Instituut voor Plasmafysica, Rijnhuizen, Edisonbaan 14, 3439 MN Nieuwegein, The Netherlands
57. Library, Institute of Plasma Physics, Nagoya University, Chikusa-ku, Nagoya 464, Japan
58. Library, International Centre for Theoretical Physics, P.O. Box 586, I-34100 Trieste, Italy
59. Library, Centro Richerche Energia Frascati, C.P. 65, I-00044 Frascati, Rome, Italy
60. Library, Plasma Physics Laboratory, Kyoto University, Gokasho, Uji, Kyoto, Japan
61. Plasma Research Laboratory, Australian National University, P.O. Box 4, Canberra, A.C.T. 2000, Australia
62. Library, Japan Atomic Energy Research Institute, Tokai, Naka-gun, Ibaraki, Japan
63. Library, Japan Atomic Energy Research Institute, Mukouyama, Naka-machi, Naka-gun, Ibaraki-ken, 311-02 Japan
64. G. A. Eliseev, I. V. Kurchatov Institute of Atomic Energy, P. O. Box 3402, 123182 Moscow, U.S.S.R.

65. V. A. Glukhikh, Scientific-Research Institute of Electro-Physical Apparatus, 188631 Leningrad, U.S.S.R.
66. I. Shpigel, Institute of General Physics, U.S.S.R. Academy of Sciences, Ulitsa Vavilova 38, Moscow, U.S.S.R.
67. D. D. Ryutov, Institute of Nuclear Physics, Siberian Branch of the Academy of Sciences of the U.S.S.R., Sovetskaya St. 5, 630090 Novosibirsk, U.S.S.R.
68. V. T. Tolok, Kharkov Physical-Technical Institute, Academical St. 1, 310108 Kharkov, U.S.S.R.
69. Library, Academia Sinica, P.O. Box 3908, Beijing, China (PRC)
70. D. Crandall, Experimental Plasma Research Branch, Division of Development and Technology, Office of Fusion Energy, Office of Energy Research, ER-542 Germantown, U.S. Department of Energy, Washington, DC 20545
71. N. A. Davies, Office of the Associate Director, Office of Fusion Energy, Office of Energy Research, ER-51 Germantown, U.S. Department of Energy, Washington, DC 20545
72. D. B. Nelson, Director, Division of Applied Plasma Physics, Office of Fusion Energy, Office of Energy Research, ER-54 Germantown, U.S. Depart ment of Energy, Washington, DC 20545
73. E. Oktay, Division of Confinement Systems, Office of Fusion Energy, Office of Energy Research, ER-55 Germantown, U.S. Department of Energy, Washington, DC 20545
74. W. Sadowski, Fusion Theory and Computer Services Branch, Division of Applied Plasma Physics, Office of Fusion Energy, Office of Energy Research, ER-541 Germantown, U.S. Department of Energy, Washington, DC 20545
75. P. M. Stone, Fusion Systems Design Branch, Division of Development and Technology, Office of Fusion Energy, Office of Energy Research, ER-532 Germantown, U.S. Depart ment of Energy, Washington, DC 20545
76. J. M. Turner, International Programs, Office of Fusion Energy, Office of Energy Research, ER-52 Germantown, U.S. Depart ment of Energy, Washington, DC 20545
77. R. E. Mickens, Atlanta University, Department of Physics, Atlanta, GA 30314
78. M. N. Rosenbluth, University of San Diego, San Diego, CA 92210
79. Duk-In Choi, Department of Physics, Korea Advanced Institute of Science and Technology, P.O. Box 150, Chong Ryang-Ri, Seoul, Korea
80. Library of Physics Department, University of Ioannina, Ioannina, Greece
81. Theory Department Read File, c/o D. W. Ross, University of Texas, Institute for Fusion Studies, Austin, TX 78712

82. Theory Department Read File, Plasma Fusion Center, NW 16-202, Massachusetts Institute of Technology, Cambridge, MA 02139
83. Theory Department Read File, c/o R. White, Princeton Plasma Physics Laboratory, P.O. Box 451, Princeton, NJ 08544
84. Theory Department Read File, c/o L. Kovrizhnykh, Lebedev Institute of Physics, Academy of Sciences, 53 Leninsky Prospect, 117924 Moscow, U.S.S.R.
85. Theory Department Read File, c/o B. B. Kadomtsev, I. V. Kurchatov Institute of Atomic Energy, P.O. Box 3402, 123182 Moscow, U.S.S.R.
86. Theory Department Read File, c/o T. Kamimura, Institute of Plasma Physics, Nagoya University, Nagoya 464, Japan
87. Theory Department Read File, c/o C. Mercier, Departemente de Recherches sur la Fusion Controlee, B.P. No. 6, F-92260 Fontenay-aux-Roses (Seine), France
88. Theory Department Read File, c/o T. E. Stringer, JET Joint Undertaking, Abingdon, Oxfordshire OX14 3EA, United Kingdom
89. Theory Department Read File, c/o R. Briscoe, Culham Laboratory, Abingdon, Oxfordshire OX14 3DB, United Kingdom
90. Theory Department Read File, c/o D. Biskamp, Max-Planck-Institut für Plasmaphysik, Boltzmannstrasse 2, D-8046 Garching, Federal Republic of Germany
91. Theory Department Read File, c/o T. Takeda, Japan Atomic Energy Research Institute, Tokai Establishment, Tokai-mura, Naka-gun, Ibaraki-ken, Japan
92. Theory Department Read File, c/o J. Greene, GA Technologies, Inc., P.O. Box 85608, San Diego, CA 92138
93. Theory Department Read File, c/o L. D. Pearlstein, L-630, Lawrence Livermore National Laboratory, P.O. Box 5511, Livermore, CA 94550
94. Theory Department Read File, c/o R. Gerwin, CTR Division, Los Alamos National Laboratory, P.O. Box 1663, Los Alamos, NM 87545
95. C. De Palo, Library, Associazione EURATOM-ENEA sulla Fusione, CP 65, I-00044 Frascati (Roma), Italy

96–211. Given distribution according to TIC-4500, Magnetic Fusion Energy (Category Distribution UC-20g, Theoretical Plasma Physics)